

Planck 2013 results X. Energetic particle effects: characterization, removal, and simulation.

Planck Collaboration: P. A. R. Ade⁸⁰, N. Aghanim⁵⁵, C. Armitage-Caplan⁸⁴, M. Arnaud⁶⁷, M. Ashdown^{64,6}, F. Atrio-Barandela¹⁸, J. Aumont⁵⁵, C. Baccigalupi⁷⁹, A. J. Banday^{87,10}, R. B. Barreiro⁶¹, E. Battaner⁸⁸, K. Benabed^{56,86}, A. Benoît⁵³, A. Benoit-Lévy^{24,56,86}, J.-P. Bernard¹⁰, M. Bersanelli^{33,46}, P. Bielewicz^{87,10,79}, J. Bobin⁶⁷, J. J. Bock^{62,11}, J. R. Bond⁹, J. Borrill^{14,81}, F. R. Bouchet^{56,86}, M. Bridges^{64,6,59}, M. Bucher¹, C. Burigana^{45,31}, J.-F. Cardoso^{68,1,56}, A. Catalano^{69,66}, A. Challinor^{59,64,12}, A. Chamballu^{67,15,55}, L.-Y. Chiang⁵⁸, H. C. Chiang^{26,7}, P. R. Christensen^{75,36}, S. Church⁸³, D. L. Clements⁵¹, S. Colombi^{56,86}, L. P. L. Colombo^{23,62}, F. Couchot⁶⁵, A. Coulais⁶⁶, B. P. Crill^{62,76}, A. Curto^{6,61}, F. Cuttaia⁴⁵, L. Danese⁷⁹, R. D. Davies⁶³, P. de Bernardis³², A. de Rosa⁴⁵, G. de Zotti^{42,79}, J. Delabrouille¹, J.-M. Delouis^{56,86}, F.-X. Désert⁴⁹, J. M. Diego⁶¹, H. Dole^{55,54}, S. Donzelli⁴⁶, O. Doré^{62,11}, M. Douspis⁵⁵, X. Dupac³⁸, G. Efstathiou⁵⁹, T. A. Enblin⁷², H. K. Eriksen⁶⁰, F. Finelli^{45,47}, O. Forni^{87,10}, M. Frailis⁴⁴, E. Franceschi⁴⁵, S. Galeotta⁴⁴, K. Ganga¹, M. Giard^{87,10}, D. Girard⁶⁹, Y. Giraud-Héraud¹, J. González-Nuevo^{61,79}, K. M. Górski^{62,90}, S. Gratton^{64,59}, A. Gregorio^{34,44}, A. Gruppuso⁴⁵, F. K. Hansen⁶⁰, D. Hanson^{73,62,9}, D. Harrison^{59,64}, S. Henrot-Versillé⁶⁵, C. Hernández-Monteagudo^{13,72}, D. Herranz⁶¹, S. R. Hildebrandt¹¹, E. Hivon^{56,86}, M. Hobson⁶, W. A. Holmes⁶², A. Hornstrup¹⁶, W. Hovest⁷², K. M. Huffenberger⁸⁹, T. R. Jaffe^{87,10}, A. H. Jaffe⁵¹, W. C. Jones²⁶, M. Juvela²⁵, E. Keihänen²⁵, R. Keskitalo^{22,14}, T. S. Kisner⁷¹, R. Kneissl^{37,8}, J. Knoche⁷², L. Knox²⁷, M. Kunz^{17,55,3}, H. Kurki-Suonio^{25,40}, G. Lagache⁵⁵, J.-M. Lamarre⁶⁶, A. Lasenby^{6,64}, R. J. Laureijs³⁹, C. R. Lawrence⁶², R. Leonardi³⁸, C. Leroy^{55,87,10}, J. Lesgourgues^{85,78}, M. Liguori³⁰, P. B. Lilje⁶⁰, M. Linden-Vørnle¹⁶, M. López-Caniego⁶¹, P. M. Lubin²⁸, J. F. Macías-Pérez⁶⁹, N. Mandolesi^{45,5,31}, M. Maris⁴⁴, D. J. Marshall⁶⁷, P. G. Martin⁹, E. Martínez-González⁶¹, S. Masi³², S. Matarrese³⁰, F. Matthai⁷², P. Mazzotta³⁵, P. McGehee⁵², A. Melchiorri^{32,48}, L. Mendes³⁸, A. Mennella^{33,46}, M. Migliaccio^{59,64}, A. Miniussi⁵⁵, S. Mitra^{50,62}, M.-A. Miville-Deschênes^{55,9}, A. Moneti⁵⁶, L. Montier^{87,10}, G. Morgante⁴⁵, D. Mortlock⁵¹, S. Mottet⁵⁶, D. Munshi⁸⁰, J. A. Murphy⁷⁴, P. Naselsky^{75,36}, F. Nati³², P. Natoli^{31,4,45}, C. B. Netterfield²⁰, H. U. Nørgaard-Nielsen¹⁶, F. Novello⁶³, D. Novikov⁵¹, I. Novikov⁷⁵, S. Osborne⁸³, C. A. Oxborrow¹⁶, F. Paci⁷⁹, L. Pagano^{32,48}, F. Pajot⁵⁵, D. Paoletti^{45,47}, F. Pasian⁴⁴, G. Patanchon¹, O. Perdereau⁶⁵, L. Perotto⁶⁹, F. Perrotta⁷⁹, F. Piacentini³², M. Piat¹, E. Pierpaoli²³, D. Pietrobon⁶², S. Plaszczynski⁶⁵, E. Pointecouteau^{87,10}, G. Polenta^{4,43}, N. Ponthieu^{55,49}, L. Popa⁵⁷, T. Poutanen^{40,25,2}, G. W. Pratt⁶⁷, G. Prézeau^{11,62}, S. Prunet^{56,86}, J.-L. Puget⁵⁵, J. P. Rachen^{21,72}, B. Racine¹, M. Reinecke⁷², M. Remazeilles^{55,1}, C. Renault⁶⁹, S. Ricciardi⁴⁵, T. Riller⁷², I. Ristorcelli^{87,10}, G. Rocha^{62,11}, C. Rosset¹, G. Roudier^{1,66,62}, B. Rusholme⁵², L. Sanselme⁶⁹, D. Santos⁶⁹, A. Sauvé^{87,10}, G. Savini⁷⁷, E. P. S. Shellard¹², L. D. Spencer⁸⁰, J.-L. Starck⁶⁷, V. Stolyarov^{6,64,82}, R. Stompór¹, R. Sudiwala⁸⁰, F. Sureau⁶⁷, D. Sutton^{59,64}, A.-S. Suur-Uski^{25,40}, J.-F. Sygnet⁵⁶, J. A. Tauber³⁹, D. Tavagnacco^{44,34}, L. Terenzi⁴⁵, L. Toffolatti^{19,61}, M. Tomasi⁴⁶, M. Tristram⁶⁵, M. Tucci^{17,65}, G. Umata⁴¹, L. Valenziano⁴⁵, J. Valiviita^{40,25,60}, B. Van Tent⁷⁰, P. Vielva⁶¹, F. Villa⁴⁵, N. Vittorio³⁵, L. A. Wade⁶², B. D. Wandelt^{56,86,29}, D. Yvon¹⁵, A. Zacchei⁴⁴, A. Zonca²⁸

(Affiliations can be found after the references)

Received XX, 2013; accepted XX, 2014

ABSTRACT

This paper presents the detection, interpretation and removal of the signal resulting from interactions of high energy particles with the *Planck* High Frequency Instrument (HFI). These interactions fall into two categories, heating the 0.1 K bolometer plate and glitches in each detector time stream. Glitch shapes are not simple single pole exponential decays and fall into three families. The glitch shape for each family has been characterized empirically in flight data and removed from the detector time streams. The spectrum of the count rate per unit energy is computed for each family and a correspondence to where on the detector the particle hit is made. Most of the detected glitches are from galactic protons incident on the Si die frame supporting the micromachined bolometric detectors. At HFI, the particle flux is $\sim 5 \text{ cm}^{-2} \text{ s}^{-1}$ and is dominated by protons incident on the spacecraft with an energy $> 39 \text{ MeV}$, leading to a rate of typically one event per second and per detector. Different categories of glitches have different signature in timestreams. Two of the glitch types have a low amplitude component that decays over nearly 1 second. This component produces an excess noise if not properly removed from the time ordered data. We have used a glitch detection and subtraction method based on the joint fit of population templates. The application of this novel glitch removal method removes excess noise from glitches. Using realistic simulations, we find this method does not introduce signal bias.

Key words. Cosmology: observations – Cosmic background radiation – Surveys – Space vehicles: instruments – Instrumentation: detectors – Space radiation: particle environment

1. Introduction

This paper, one of a set associated with the 2013 release of data from the *Planck*¹ mission (Planck Collaboration I 2013), describes the detection of high energy particles with the 0.1 K in-

strument and bolometric detectors in the *Planck* High Frequency Instrument (HFI) (Lamarre et al. 2010) and removal of these systematic effects from the millimeter and sub-millimeter signals. Bolometers (Holmes et al. 2008), such as those used in HFI on *Planck*, are phonon mediated thermal detectors with finite response time to changes in the absorbed optical power. The

¹ *Planck* (<http://www.esa.int/Planck>) is a project of the European Space Agency (ESA) with instruments provided by two scientific consortia funded by ESA member states (in particular the lead countries France and Italy), with contributions from NASA (USA) and

telescope reflectors provided by a collaboration between ESA and a scientific consortium led and funded by Denmark.

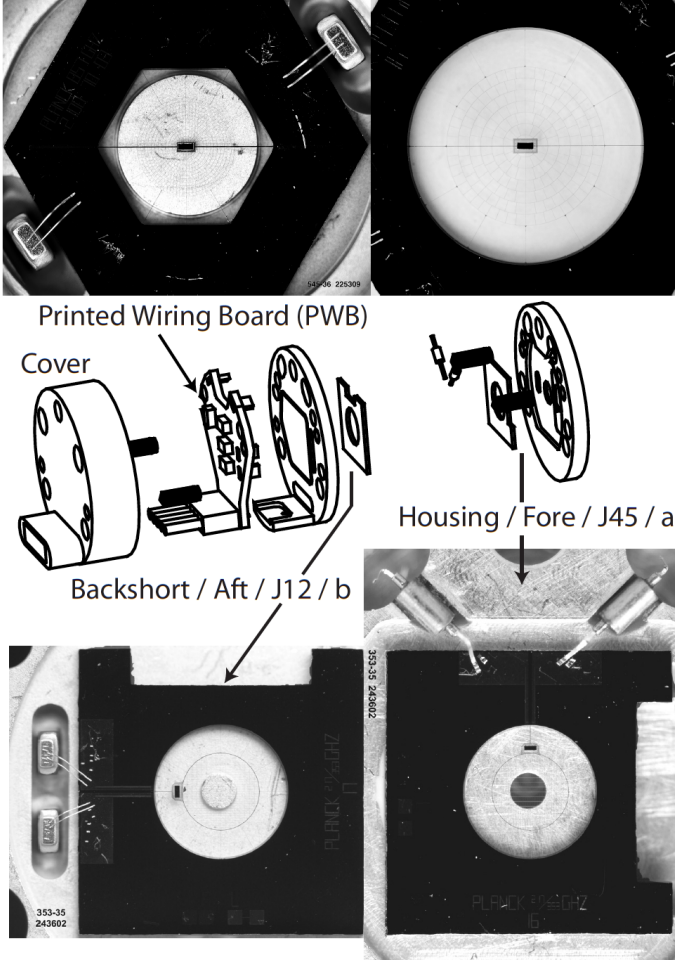


Fig. 1. Top left and right: Completed multimode 545GHz and single mode 143GHz SWB bolometer modules. Middle: An exploded view of the assembly of a PSB. Alignment pins, shown in solid black, fix the aft and fore bolometer assemblies to an angular precision of $< 0.1^\circ$. The SWB assembly is similar to the PSB aft bolometer assembly and does not include a feedhorn aperture integrated with the module package. Bottom: A PSB pair epoxied in the module parts prior to mating. To the right, the feedhorn aperture can be seen through the fore bolometer in the housing. To the left, the 1/4 wave backshort can be seen through the aft bolometer absorber mesh.

bolometer consists of a micromachined silicon nitride (Si-N) mesh absorber with a Ge thermistor suspended from the Si die frame. Each bolometer is mounted to a metal housing which are assembled into two types of bolometer modules shown in Figure 1; a Spider Web Bolometer (SWB) which detects total power and a Polarized Sensitive Bolometer (PSB) (Jones et al. 2007). In the PSB, there are two bolometers to measure independently power in each of the two linear polarizations, as shown in Figure 1. The bolometers are mounted to a copper-plated stainless steel plate cooled to 0.1K and stabilized to a few microK of the temperature set point. Two ‘dark’ bolometer modules are blanked off at the 0.1K plate and are used to monitor systematic effects. The 0.1 K bolometer plate is surrounded by a $\sim 1.5\text{mm}$ thick aluminum box cooled to 4.5 K. Light is coupled into each bolometer module using a feedhorn and filter stack at 4.5 K and 1.5 K respectively (Lamarre et al. 2010).

At L2, high energy particles from the sun and a galactic sources, primarily, protons, electrons and helium nuclei, are in-

cident on the spacecraft. This particle flux causes two main effects in HFI that have been reported previously. There is a time variable thermal load on the 0.1K plate (Planck Collaboration II 2011) and a significant rate of glitches in the bolometric signal (Planck HFI Core Team 2011). In this paper, we report on the evolution of these effects over the entire mission, from July 3, 2009 through January 14, 2012 and on the analysis technique used to remove the effect of glitches from the data. Three families of glitches, long, short and slow (or longer as named in Planck HFI Core Team 2011), were found by comparing and stacking many events. We present the coincident counts, energy distribution, total counts and variations of glitch shapes within each family. These data taken together allow identification of the physical cause of the glitch events for two of the types. Long glitches are energy absorption events in the silicon die and short glitches are events in the optical absorbing grid or Ge thermistor. Experimental evidence obtained using beam line and lab tests using spare HFI bolometers supports these conclusions (Catalano et al. 2013; Planck Collaboration II 2011). The cause of the slow glitches, however, has not been identified. The new analysis presented here employs a joint fitting and removal of these three glitch types. We show that this technique improves the noise performance of HFI. We report on rare effects not previously reported, including the response of the instrument to solar flares, secondary showers and large high energy events. We have simulated the effect of the glitches on the data quality and find that systematic biases are small, $< 10^{-4}$ compared to the cosmological signal.

2. Glitch characterisation from bolometer data

As reported previously (Planck HFI Core Team 2011), the glitch rate in *Planck* HFI is about 1 per second. To remove glitches from the data time streams of many instruments with bolometric detectors, (Crill et al. 2003; Masi et al. 2006), the instrument transfer function is deconvolved from the data. This has the benefit of increasing the signal to noise on each glitch which minimizes the fraction of flagged data. The populations of glitches in *Planck* HFI is unusual. Three distinct families of glitch transfer functions, shown in Figure 2, are found in the data. The three families of events, ‘short’, ‘long’ and ‘slow’ are differentiated by their decaying time constants and amplitudes. Of these, the long glitches dominate the total rate. This type, however, has a significant amplitude over more than 1 second. Therefore, simple flagging and removal of these glitches would lead to an unacceptably large loss of data. To avoid such data loss, precise glitch templates, need to be subtracted from the time ordered data. To do this, we take advantage of the excellent pointing accuracy (Planck Collaboration I 2011) and redundancy of the scan strategy and have adopted a method that iterates between estimates of the signal from the sky and signal from the glitches (Planck HFI Core Team 2011). A key to the effectiveness of the method is a comprehensive understanding of the three families of glitches and stability of these families over the course of the mission. In this section, we describe the general features of templates of each of the three glitch families obtained from stacking many normalized glitches and the general features of the glitch templates derived from fitting the normalized decay profile with the sum of 4 exponentials Planck Collaboration VII (2013).

2.1. Short glitches

The short events have a rising time constant well within the sampling period of $\sim 5\text{ms}$ and then a fast decay. The highest am-

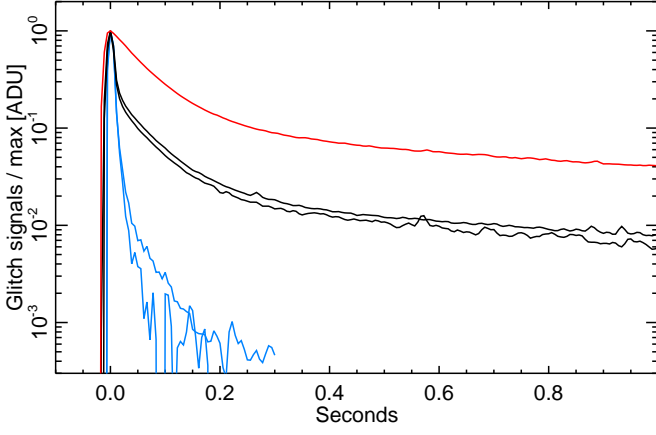


Fig. 2. Different types of glitches found in bolometer data. Examples for three distinct families of glitch transfer functions displayed for a typical the PSB-a bolometer. Events typical of the blue curves are called short events, those typical of the black curves are called long, and those of the red are called slow. Typical variation in the shape within each family is shown for short and long glitches.

plitude glitches are short glitches. The short glitch template for each bolometers is shown in Figure 3. We see small variability in the averaged short glitch template depending on the detector. The shortest exponential decay has a time constant similar to the fast part of the optical transfer function with the three additional terms, or tail, having a very low amplitude $< 10^{-2}$ relative to the peak and intermediate time constants of typically 40 ms, 400 ms and 2 seconds. The 2-second decaying signal is $\sim 10^{-4}$ and was detected only after stacking short glitches measured over the entire mission. We have observed some similarities between the transfer function of short glitches and the optical transfer functions (Catalano et al. 2013). The amplitude of the tail is variable from event to event, but the amplitude of the tail is small enough such that its variability does not affect the processing of data. Moreover, we have found the existence of essentially two sub-categories of short glitches, one of each is shown in Figure 2, that can be distinguished by the amplitude of the tails. In fact, the tail is smaller for higher energy events and larger for lower energy events with a variation of a factor 2. The time constants, as well as amplitudes resulting from the fit of three exponentials on short glitch measurements are given in Figure 4 for all bolometers. The fit has been performed after stacking events with amplitudes between 1200 and 2400 sigmas of the noise, with corresponds energies of the transition between the two sub-categories of short glitches. The 2 second time constant is not included in the template fit. We observe some scatter of the values across bolometers which are reflecting more the degeneracies in the fit of the different time constants and amplitudes than variations of the template shape between bolometers. A careful study of degeneracies of parameter fitting is performed in Planck Collaboration VII (2013) for the transfer function analysis.

2.2. Long glitches

The long glitches are on average lower amplitude than short glitches but dominate the rate over other categories of glitches by more than an order of magnitude. The rising time constant is very fast and within the sampling period as for short glitches.

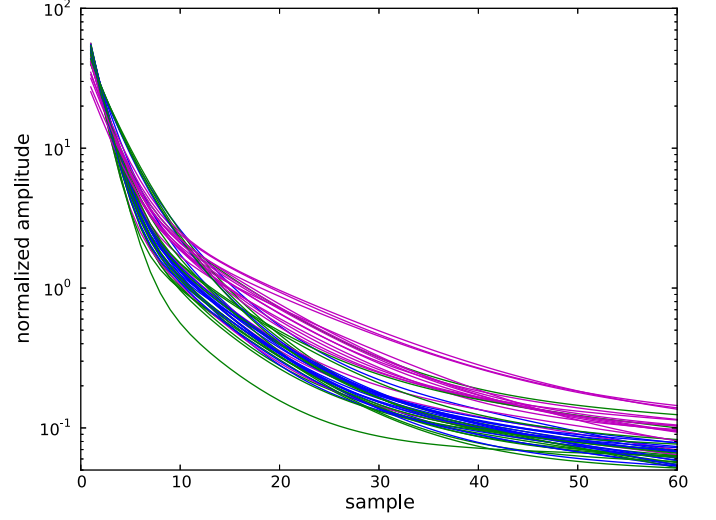


Fig. 3. Short glitch templates for all detectors. Blue color is for PSB-a, green for PSB-b and violet for SWB.

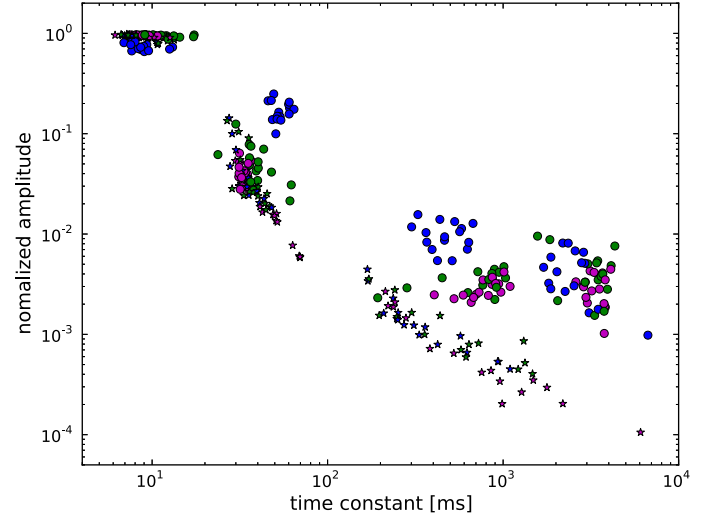


Fig. 4. Parameters of the glitch templates for all bolometers. Left: short glitch template, right: long glitch template. The type of bolometers is indicated by color (blue = PSB-a, green=PSB-b, magenta= SWB) and the type of glitch by symbol (circle = long glitches, stars = short ones). Values quoted are obtained after fitting exponentials on templates estimated by stacking large number of events. A three-point filter was applied to the data prior to the fit of exponentials. There are degeneracies in the fit of the different parameters, this is studied in detail in Planck Collaboration VII (2013) for the similar problem of transfer function fitting.

The shortest exponential decay has a time constant similar to the fast part of the optical transfer function, followed by a tail with a much larger amplitude than for the short glitches. In Figure 5 long glitch templates are shown for several bolometers. As with the short glitches they are estimated by the stacking of large number of events and fit to a sum of 4 exponential terms.

The slow tail has typical time constants of 50 ms, 500 ms and 2 seconds for PSB-a bolometers and 35 ms, 500 ms and 2s for PSB-b and SWB bolometers. The intermediate time constant of 35 to 50 ms starts with an amplitude relative to the peak of $\approx 6\%$ for PSB-a and of $\approx 3\%$ for PSB-b and SWB bolometers. The

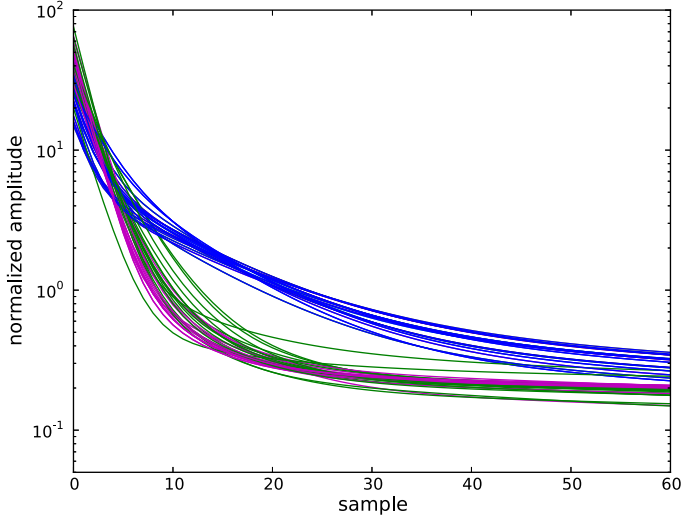


Fig. 5. Long glitch templates for all detectors. Blue color is for PSB-a, green for PSB-b and violet for SWB.

long time constants of ≈ 500 ms and 2 seconds have an amplitude which is about 0.2% of the event peak. Given that most of the glitches are these long events in HFI data, the tail would cause excess power in the noise if not carefully removed.

The most striking feature in Figure 5 is that the intermediate time constant is significantly slower and lower in amplitude for PSB-b and SWB as compared to PSB-a. The component of the tail with the longest time constant, of the order of 2 s, has a similar amplitude for all bolometers. The time constants and amplitudes are given in Figure 4 for all bolometers.

We do not observe significant change in the time constants of the long glitch tail from glitch to glitch. However, the relative amplitude of the long tail with respect to the fast part show very significant dispersion. This is illustrated in Figure 6, where we show the distribution of the peak glitch amplitude as a function of the relative amplitude of the glitch tail for a typical PSB-a and PSB-b. If the long glitch shape was identical for all glitches, we would observe a distribution along a vertical axis centered at unity, with a width fixed by the measurement errors. Instead, we observe that the width of the distribution is larger than expected from just increasing signal to noise for increasing glitch peak amplitude. This intrinsic scatter in the long tail amplitude can only be partly due to the signal averaging on the sample affecting mainly the peak of the glitch, and decreasing the amplitude by a factor which depend on the timing of the glitch impact within a sample period (Lamarre et al. 2010). Moreover, the distribution of slow part amplitude is for some bolometer double-peaked. Also, a small proportion of events have an amplitude of the fast part relative to the slow part which is different than for most long glitches. In particular, slightly less than 10% of events have a smaller amplitude tail than long glitches and about 0.5% have a higher tail. The events close to zero in the x-axis, are a small quantity events with low enough amplitude that short and long event cannot be distinguished.

Moreover, we observe that the ratio between the amplitude of the slow tail and the peak amplitude of long glitches, is not a constant with respect to the peak amplitude of glitches. Higher energy events have a relatively higher longer tail. This non-linearity is seen in Figure 6, as a slight curvature of a the subset of high energy events highlighted by a dashed line. We have corrected for this nonlinearity by modelling the peak amplitude as a quadratic function of the tail amplitude. By comparing the non-

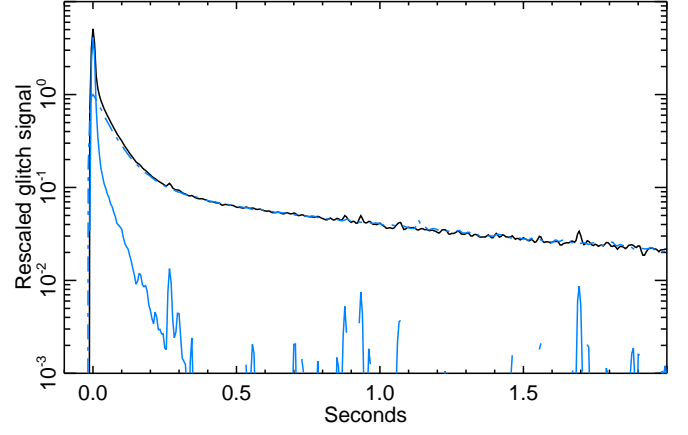


Fig. 7. Comparison of a long glitch (black) and a slow glitch (dot dashed blue). For this plot, the two high energy events were rescaled to match after 200 ms. The difference is shown in blue.

linearity functions between bolometers, we observe a systematic difference between PSB-a and PSB-b/SWB bolometers. The non-linearity for PSB-a corresponds to a factor 2 between the lowest and the highest energies of detected events, and is slightly stronger than that PSB-b and SWB which is a factor 1.5. Apart from this non-linearity, which is accounted in the glitch subtraction method, we have checked that there is no dependency of the time constants of the slow tail with respect to the energy of the events, as illustrated by Figure 25 showing the stacking of events for different energy windows.

2.3. Slow glitches

For PSB-a bolometers only, the distribution of glitch peak amplitude to tail amplitude has a significant extra peak at $\hat{a}_l/g_{\max} \sim 6$. This extra peak is the signature of the slow glitches. The slow glitches have a rising time comparable to the optical time constant; much slower than the 2 other glitch families. The tail of the slow glitch is similar to that for a long glitch. In Figure 7 shows the comparison of a high amplitude long glitch event with a slow glitch. The intermediate time constant which is of the order of 50 ms for long glitches is slightly but significantly larger for slow glitches as can be seen Figure 7. The two tails are proportional to a very good accuracy after ≈ 200 ms after the peak amplitude. Even with these differences, the long glitch template for a given bolometer is a good proxy of the slow glitches in the same bolometer.

2.4. Evolution of the Glitch Rate over the Mission

Over the course of the whole mission, the rate for each type of glitch decreases, as shown in Figure 8. This decrease is universal for all bolometers as shown in Figure 9. The signal from diode sensor TC2, the most shielded of the 3 diodes in the Standard Radiation Event Monitor (SREM, Mohammadzadeh et al. 2003) located on the sun side of the *Planck* spacecraft, follows a similar trend with time as shown in Figure 10. This trend is predicted for galactic cosmic rays modulated by the heliosphere of the sun (Gleeson & Axford 1968; Bobik et al. 2012) and is observed by ground stations on earth and other spacecraft in the solar system. (Usokin et al. 2011; Wiedenbeck et al. 2005; Adriana 2011). Taken together, the glitch rate, SREM diode signal and data from other sources, the source of glitches in the HFI bolometers is

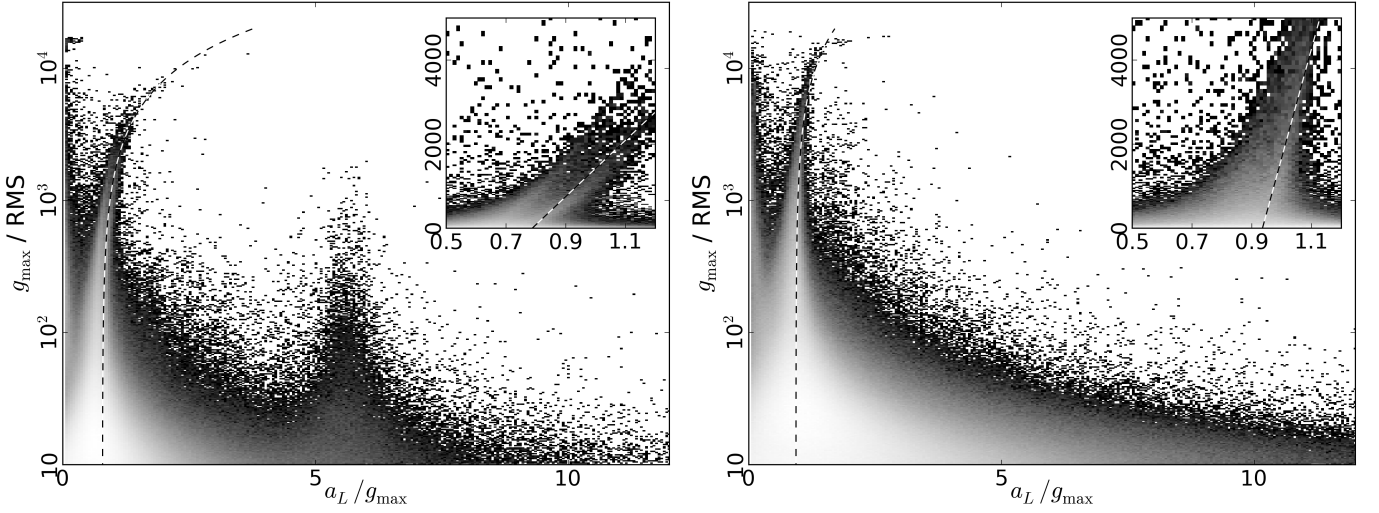


Fig. 6. Distribution of glitches with respect to the log of their peak amplitude and of ratio of the slow tail to fast part amplitudes. This last ratio is estimated by \hat{a}_l/g_{\max} , where \hat{a}_l is the fitted amplitude of the long glitch template (which has been normalized for long) and g_{\max} is the glitch maximum. Left and right panels are for one of the PSB-a (143-3a) and one of the PSB-b (143-3b) detectors, respectively. The same distributions are shown in linear scale in the upper left corner of the windows. The dash lines indicate the observed non-linearity of the amplitude of the slow part of long glitches relative to the peak amplitudes. Long glitches populate the distribution along those lines and short glitches populate the distribution along the vertical axis close to zero. Slow glitches are clearly visible in the distribution centered at around 6, for the PSB-a, and are absent for PSB-b bolometers. The distribution of template amplitudes at the limit of weak glitch peak amplitudes is wider for PSB-b due to larger estimation errors, as long glitches for PSB-b (and SWB) have lower amplitude intermediate time constants than for PSB-a. For some bolometer (as for this PSB-a) we observe a double peaked distribution of long glitch template amplitudes.

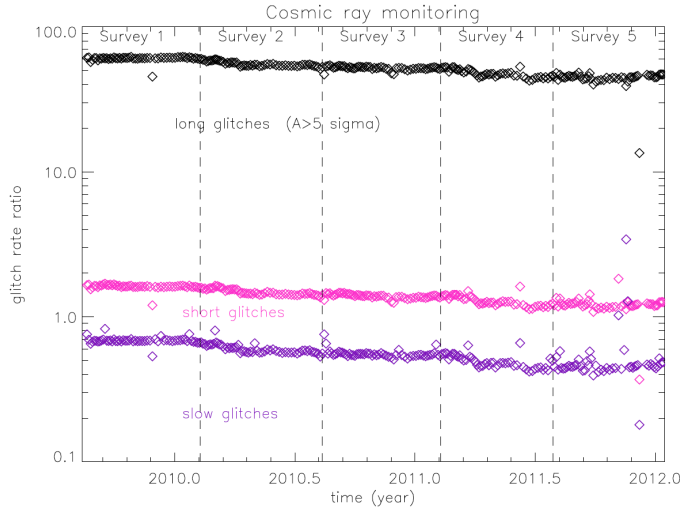


Fig. 8. Mean rate of the three categories of glitches long, short and slow glitches. These rates are computed using the 52 bolometers for long and short glitches, the 16 PSB-a bolometers for slow glitches.

from galactic cosmic rays. Indeed, other sources, such as on-board radioactivity and solar protons as detected by the mirror on WMAP (Jarosik et al. 2007) were suspected to contribute to the glitch rate, but would not follow the trends with time that are observed.

2.5. Population counts

Figure 11 shows the distribution dN/dE of the three populations of glitches as a function of the amplitude of events in signal to

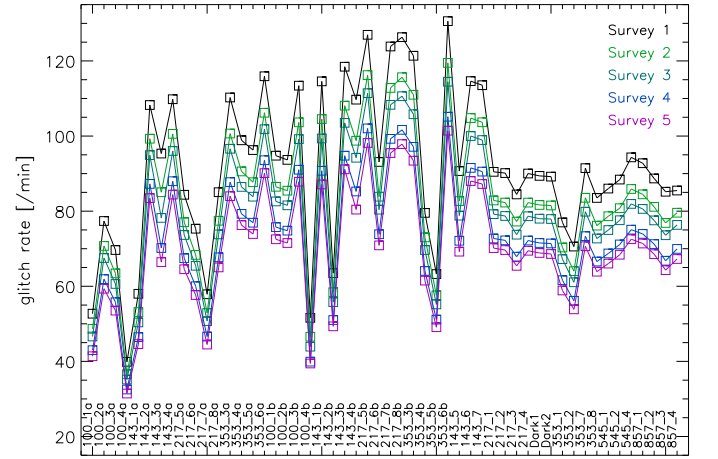


Fig. 9. Glitch rate per bolometer. Each point is the mean value during a survey (6 months).

noise units for one of the detectors. The type of each event is determined from the output of the method detailed in 4.1. We can see that long glitch events are dominant at lower amplitudes while short events dominate at higher amplitudes. The separation between short and long events is not very efficient below ≈ 20 sigmas of the noise as the tail of long glitches, used to distinguish between the two types of events, is barely detectable. Nevertheless, we will see later that long glitches are dominant at lower amplitudes. Long glitches are dominant in the overall counts, and the tail of those events is responsible of the noise excess at frequencies between 0.001 Hz and 0.1 Hz, requiring their subtraction in order to reach the expected level of noise (see Planck HFI Core Team 2011, and Section 4.2). The distribution of long glitches is well fitted by a steep power law of

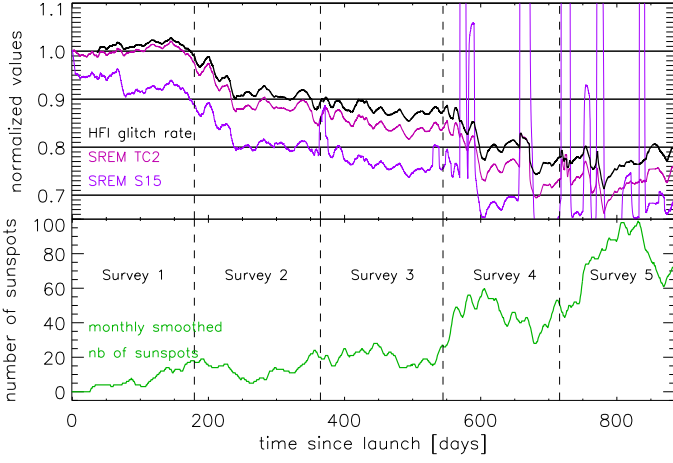


Fig. 10. Top : Normalized glitch rate (black line), cosmic rays flux measured by the SREM for deposited $E > 3$ MeV in purple, and $E > 0.085$ MeV in pink, as a function of time. Bottom : monthly smoothed number of sun spots.

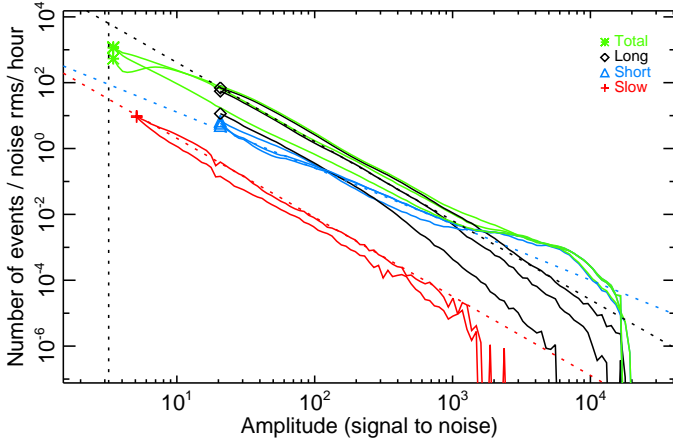


Fig. 11. Distributions dN/dE of the three families of glitches with respect to the peak amplitude in signal to noise units, for three different bolometers: 143-1a, 143-2a and 217-1. Blue is for the short glitch population, black is for long, red is for slow and green is for total. We have displayed populations for bolometers with very different behaviours: 143-1a has one of the least glitch rate, 143-2a and 217-1 have a high glitch rate and we observe clearly the faint-end break of the glitch counts for 217-1. This last bolometer has no slow glitches (see Section 2.3). Power laws are shown for comparison in dash lines. Indices and amplitudes of power laws are chosen to match the distribution of one of the bolometers (143-2a). Indices are -2.4 for long and slow glitches, and -1.7 for short glitches. The vertical dash line indicate the detection threshold. There is no attempt to separate the long and short glitch populations below 20 sigmas of the noise. The slow glitch spectrum is shown down to 5 sigmas.

index -2.4 between typical amplitudes of 20 and 1000 sigmas of the noise (with some variations of those values with respect to bolometers), and show breaks at both bright and faint-ends. The faint-end break is very close the glitch detection threshold fixed to 3.2 sigmas, and is detected very significantly as we will discuss later in Section 3.2. We observe that sub-millimeter channels (545 and 857 GHz) are more sensitive to long glitches. For

those detectors, we observe a peak in the differential counts at energies relatively close to the detection threshold.

We observe more differences between bolometers in the long glitch distributions than in the short glitch distributions, as can be seen in Figure 18 comparing the cumulative distributions for different bolometers and glitch families. The distribution of short glitches has a bump at amplitudes of ≈ 3000 sigmas for all bolometers from 100 to 353 GHz. There is a clear break at very high amplitudes which is mostly due to the non-linearity of detectors at those very high amplitudes and to the saturation of the analog to digital converter (ADC, see Planck Collaboration VI 2013, for a discussion about the effect on data) for a discussion about the effect on data). The bump in the distribution is not apparent in sub-millimeter detectors, but this is due to the non-linearity of detectors reducing it. For amplitudes below ≈ 1000 sigmas, the distribution of short glitches is well represented by a power law with a typical index of -1.7. Short events with an energy corresponding to the bump appear to be shorter than events corresponding to the power law. The shape of the distributions of slow and long glitches are very similar. By computing the distributions of the amplitude of the tail of both long and slow glitches, the amplitude of both distributions are also very similar.

2.6. Correlation in time

The time lapse between two consecutive glitch events exhibits an exponential shape as shown in the graph on the left in Figure 12. The absolute value of slope fitted between 1 and 2 minutes is roughly equal to the computed rate, just obtained by the number of events above 10σ in six months (right part). Clearly, all bolometer glitch distributions exhibit a Poisson law. These data are from the third survey data when the glitch rate was relatively constant and events above 10σ were selected to avoid any contamination by false events, solar flares and pile-up. We cannot check multiple simultaneous events because we cannot distinguish between a pile-up of multiple events and a single more energetic event. Thus the glitch data are compatible with pure random events which are not correlated in time and is consistent with the cause of events as individual hits by galactic cosmic ray particles.

2.7. Coincidences between detectors

We also studied the coincidences of events between bolometers. We found that the largest fraction of coincidences, $\sim 99\%$, are between PSB-a and PSB-b detector pair in the same module. The remaining $\sim 1\%$ of coincidences are particle shower events that effect a large fraction of the detectors in the focal plane in different modules. The PSB pair coincidences are discussed here and the shower events are discussed in Section 3.6. At the arrival time of each glitch detected in a PSB-a bolometer, we have measured the level of signal in the PSB-b in the same module. The glitches in PSB-a are sorted into the three categories (short, long and slow), then we compared the amplitude of the signal in PSB-b without distinction on the nature of the signal in PSB-b with the amplitude of the glitch at the maximum in PSB-a and computed a 2D histogram of the two quantities. The 2-D distribution for short, long and slow events in PSB-a are shown in Figures 13, 14 and 15, respectively. The axes indicate the log of data normalized by the noise rms. The events below 100 sigmas are not displayed since the separation between short and long glitches is uncertain.

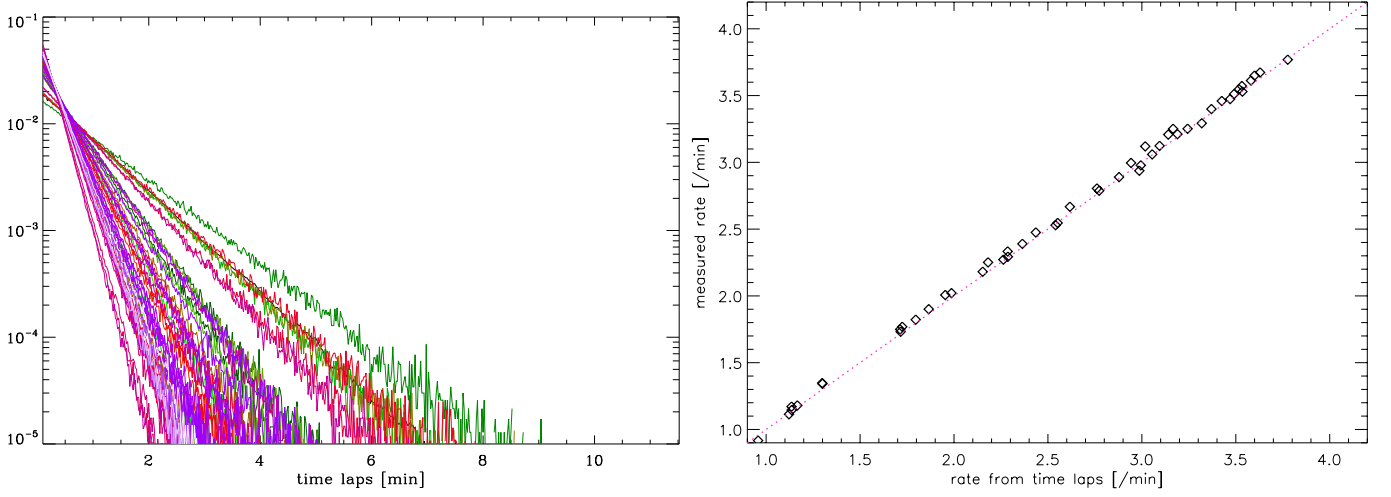


Fig. 12. Left: Histogram of time lapse between two consecutive glitch events for each bolometer normalized by total number of events. Colors are for different detectors. We observe Poisson laws as expected for random events. Right: glitch rate derived from slope of time lapse distribution compared to the mission averaged actual rate for each bolometer.

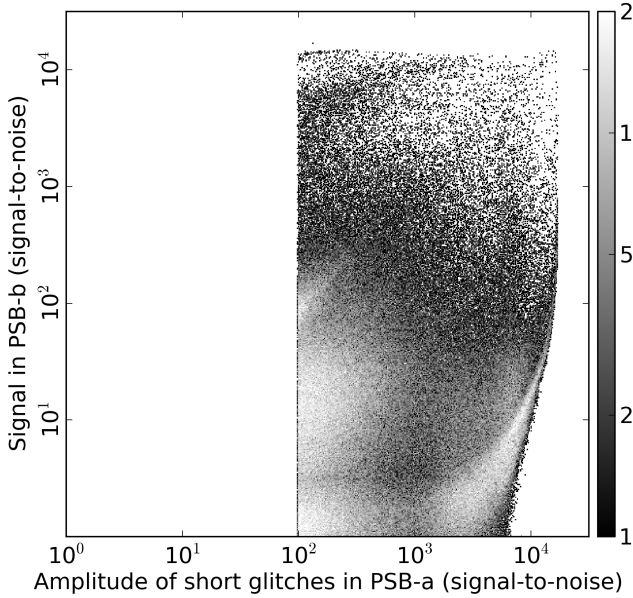


Fig. 13. Representative short glitch coincidence in a PSB pair. The x-axis represents the log of the amplitude relative to the noise of detected glitch in the PSB-a bolometer, the y-axis is the log of the value of the signal to noise in the PSB-b bolometer. The grey scale indicates the log of the number of events in logarithmic bins. Detected events are not shown below 100 sigmas in PSB-a, as we expect non-negligible contribution from long glitches, the separation between long and short being uncertain at low amplitudes. A large fraction of events are in coincidence between PSB-a and PSB-b.

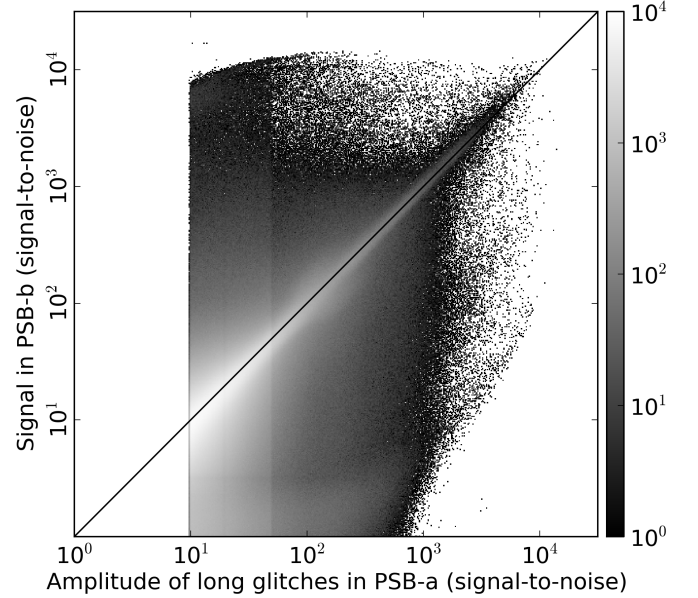


Fig. 14. Representative long glitch coincidence in a PSB pair. See description in Figure 13 caption. Events above 50 sigmas are selected such that they match the long glitch template. All events without selections are taken below 50 sigmas, as the long glitch population dominate at low amplitudes. The solid line indicates identical signal in both PSB-a and PSB-b. Most (if not all) long events as associated with significant events in PSB-b, and a large fraction have approximately the same amplitude in PSB-a and PSB-b.

We observe that most of the long glitches detected in PSB-a are also detected in coincidences in PSB-b. Furthermore, we find that for amplitudes above 300 sigmas, all glitches are detected in coincidence, as all events are seen in PSB-b above $\approx 0.3\%$ of the amplitude in PSB-a (or reversely). We cannot state this for events below 300 sigmas since a significant fraction of the counterparts in PSB-b are below the noise level. Nevertheless, the re-

sults of the coincidence analysis are compatible with the fact that all long events are in coincidence between PSB-a and PSB-b. A large fraction of these glitches is seen with an amplitude which is proportional in the two detectors, as those events lie along a line in the diagram with some intrinsic scatter, meaning that a large fraction of long glitches are coincident with the same ratio of amplitudes between 'a' and 'b'. The factor of proportionality is almost 1 in signal to noise units for this PSB pair, but can vary

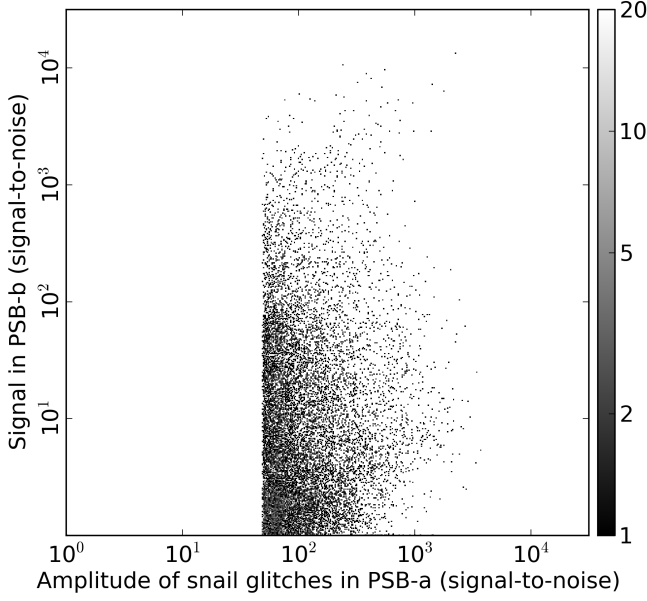


Fig. 15. Representative slow glitch coincidence in a PSB pair. See description in Figure 13 caption. No event is shown below 50 sigmas to avoid leakage from the long population. All slow glitches in PSB-a above $\approx 10^3$ sigmas are associated with significant events in PSB-b. Below $\approx 10^3$ sigmas the majority of events are associated with significant events in PSB-b, for the remaining fraction the fact that we do not see a significant signal might be a threshold effect.

between 0.25 and 4 depending on the pair (see Section 3.2 for a discussion). A very significant fraction of long glitches have counterpart in the other associated bolometer, but with a different amplitude, which is lower most of the time. The number of events in the distribution along the line of one to one correlation is of the order of 50% of the total number for events with amplitudes lower than ≈ 300 sigmas or for events above ≈ 1500 sigmas, and is of the order 35% for amplitudes in between.

The distribution of PSB-a versus PSB-b for short glitches is very different than the expected distribution for random coincidence. The expected distribution of random coincidences is evaluated by measuring the statistics of the signal in PSB-b 10 000 samples (about one minute) after each event in PSB-a, and is shown in Figure 16. In particular, we can see a wide cloud of points in the 2D histogram above 10 sigmas in PSB-b. A fraction of 50 % of the events populate the region of random coincidence. This is also shown by Figure 17 displaying the distribution of the signal in PSB-b for events in PSB-a with amplitudes between 300 and 1000 sigmas. So there are strong indications that about 50 % of short glitches are seen in coincidence between PSB-a and b. For a given amplitude of short glitch in PSB-a, we observe a wide distribution of amplitudes in PSB-b.

All very high short amplitude glitches have significant counterparts in the other bolometer at the level of $\approx 1/1000$. This is attributed to the cross-talk between the two bolometers. This will be discussed in Section 3.4.

As already stated, slow glitches are seen only in PSB-a. Nevertheless, there is a significant signal in PSB-b associated with slow glitches in PSB-a. Indeed, we can see that the distribution of counterpart in PSB-b is very different than the random distribution shown in Figure 16, which means that slow events

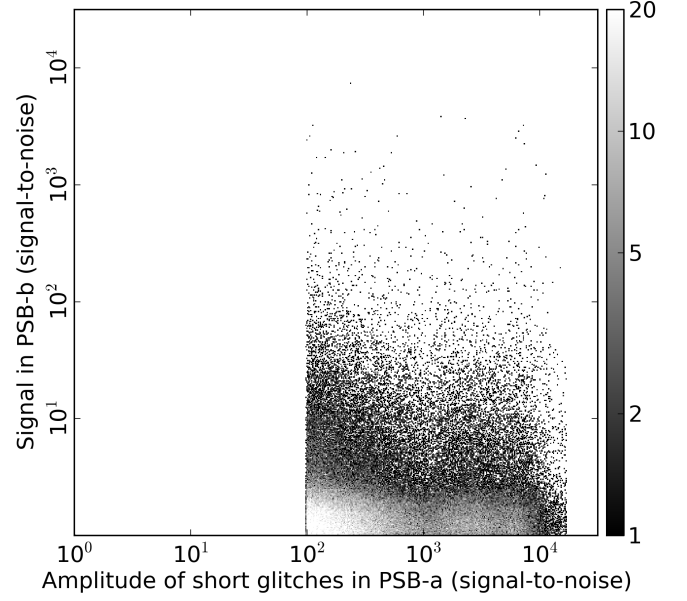


Fig. 16. Expected distribution for random coincidences. See description in Figure 13 caption. The value of the signal to noise in PSB-b for each short event in PSB-a is taken 10 000 samples after. We use short events in PSB-a such that this distribution can be directly compared to the coincidence of short glitches.

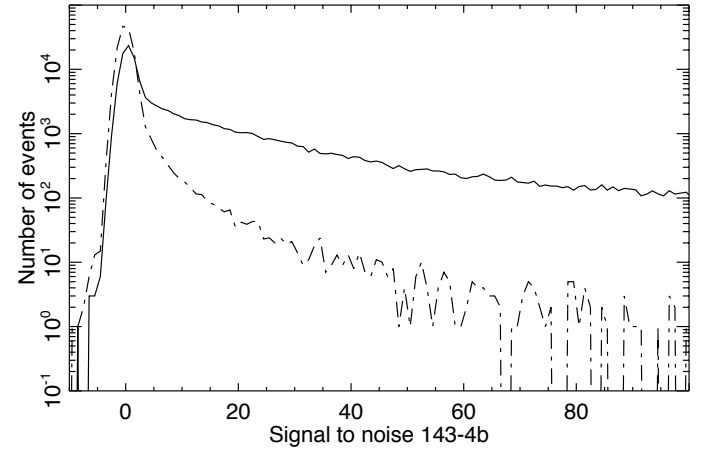


Fig. 17. Distributions of the signal values in PSB-b for short events with peak amplitudes between 300 and 1000 sigmas in PSB-a in red. Random distribution of values in PSB-b in black. The excess of the red curve over the black for amplitudes above 3 sigmas represents about 50% of the total area. Thus, at least 50% percent of the events are in coincidence between PSB-a and PSB-b.

in PSB-a are associated with signal in PSB-b. The counterparts generally have a wide range of amplitudes for a given energy of slow glitches which makes difficult the measurement of associated time constants. Visual inspection of those events allow to say that there is a variety of counterparts, some have faster decay than slow glitches and have similar rising time of ≈ 10 ms, some others (the larger energy ones) are similar to long glitches.

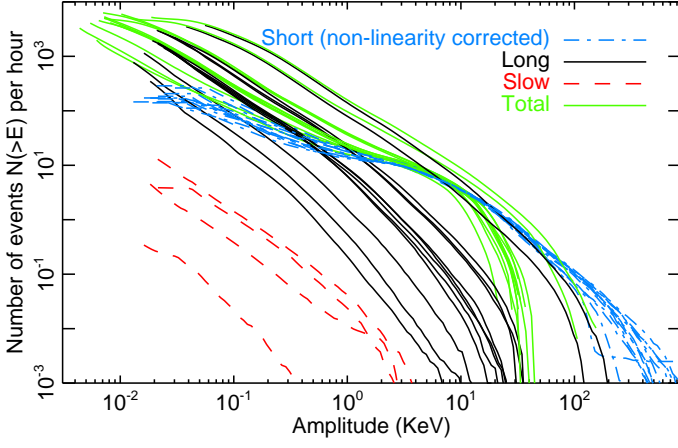


Fig. 18. Cumulative counts (in hour^{-1}) for the three categories of glitches and for several bolometers. Blue curves are for short glitches after non-linearity correction above typically 10 keV (as described in the text); black curves are for long glitches; red curves are for slow glitches; and green curves are for the total counts without non-linearity correction, which is why they lie below the blue curves. Glitches are not separated into the different categories below 10 sigmas of the noise (≈ 20 eV). All curves have been recalibrated in energy for each bolometer such that the distributions of short glitches match at energies around 10 keV (we use the same coefficient for all populations), the absolute calibration being fixed for one arbitrary detector. Notice that the distributions of short glitch match very well. There is a large scatter in the energy scaling for the other populations of glitches.

3. Interpretation

For a complete understanding of the long and short glitches observed in the HFI flight data, several laboratory tests have been performed using 23 MeV protons from a TANDEM accelerator and two radioactive alpha sources. The detailed results of all the performed tests are presented in the HFI special paper [Catalano et al. \(2013\)](#).

3.1. Interaction with the grid/thermistors

There is clear evidence that the short events are resulting from cosmic rays hitting the grid or the thermistor. Indeed, those events have a fast rising time and have a fast decay, and the transfer function built from the short glitch template (see [Catalano et al. 2013](#), for a comparison). is in good agreement with the HFI optical transfer function ([Planck Collaboration VII 2013](#)), so the energy must be deposited in the environment close to the thermistor. Figure 18 shows the cumulative counts, i.e. the number of events $N(>E)$ with an amplitude higher than a given value E per hour, of short glitches after converting the maximum amplitude of each glitch in units of energy (keV) for one reference bolometer (100-1b). The energy calibration for the other bolometers has been determined such that the cumulative distributions match the one for the reference bolometer at energies of about 10 keV. For the conversion we use the measured heat capacity of the NTD crystal + grid system, as we assume that the energy of the events is deposited in this system. The relative fitting of the energy is necessary for the comparison between bolometers because of uncertainties in the heat capacity of the system and also in how much the peak amplitude is reduced after averaging in the inter-

val of one sample with the electronics. Faster bolometers have glitches with more reduced amplitudes than slower bolometer. The effect is important for sub-millimeter channels for which the time constant is very small. We evaluated that the relative correction factor should be of the order of three between 100 and 545 GHz bolometers. We have also reconstructed and corrected the counts for high amplitudes which are affected by non-linearity (typically above ≈ 10 keV) by readjusting the values of event energies from the measurements of the slow tails of short events, which are not affected by non-linearity, instead of taking directly the peak amplitude. This allows to reconstruct the distribution more than a factor of ten above the saturation by the electronics. We can see that the counts of short events for all detectors match with a very good accuracy, around the energy bump in particular, considering the fact that no rescaling is performed on the y-axis, but only on the energy axis.

Events in the bump are expected to be associated with cosmic rays hitting the thermistor. Since thermistors are identical for all bolometers, we expect the same rates for all bolometers, this is precisely what we observe, as shown in Figure 18. Given the dimensions of the thermistors of $30 \times 100 \times 300 \mu\text{m}^3$, and the fact that typical galactic protons of energies around 1 GeV (peak of the spectrum) deposit the minimum energy of $\approx 1.47 \text{ MeV cm}^2/\text{g}$ in the Germanium, which is the minimum of the stopping power for normal incidence in the largest surface, we expect typical deposition energy of $\approx 15 \text{ keV}$ in the thermistor (the first energy being dominant since it corresponds to the largest cross-section). This is also in agreement with the energy measured experimentally, given the fact that the energy calibration is uncertain within $\approx 50\%$. The amplitude of the bump in the cumulative distribution which is of about 10 events per hour, also matches with the expectations. Indeed, by integrating the expected cosmic ray spectrum at L2, and considering that low energy particles are absorbed by the spacecraft, we can predict a total number of particles of $N \approx 5 \text{ particles/min/mm}^2$. This leads to 0.1 glitch/min on the thermistor by taking the largest surface.

The events depositing an energy of about 10 eV to 1 keV and populating the power law as seen in Figure 18, are expected to be the result of cosmic ray hitting the grid. Calculations predict a total number of events on the grid from 0.4 to 1.2 glitch/min, given that the surface from the grid varies from $4.77 \cdot 10^5 \mu\text{m}^2$ to $3.95 \cdot 10^4 \mu\text{m}^2$ depending on the bolometer. We observe a higher number of events by a factor of 2 to 4, but as well we see in the next paragraph, about half of the events for PSB bolometers might result from electrons ejected from the other grid by the impact of a cosmic ray proton. We observe some dispersion in the amplitudes of the power law distributions from bolometer to bolometer which is not obviously correlated with the area of the grids. This is attributed to the uncertainties in the intercalibration of energy to match the counts, as detailed at the beginning of this section.

The coincidences analysis, described in Section 2.7, of short glitches (Figure 13) at intermediate amplitudes which populate the power law, show that a fraction very close to 50% of events are seen in both PSB-a and PSB-b with no phase shift. A possible model is that events hitting one of the grid are ejecting some electrons hitting the other grid. The rate of 50% correlation can be explained by geometrical effects like particles coming from the top or bottom; a particle coming from the top could hit the PSB-a grid, extract electrons and project those onto the PSB-b grid, whereas a particle coming from the bottom and hitting the PSB-a grid would not project electrons on the PSB-b. The observations indicate then that nearly all events hitting one of the grid and coming from the appropriate direction must eject

electrons hitting the second grid and depositing about 10% of the energy deposited in the first grid. We also observe that some events are hitting both grids. Those appears in the cloud of points with the same amplitude in both PSB-a and b. Those represent about 2% of the events. We observe a lower coincidence rate for events at higher amplitudes corresponding to the bump. This is explained with the hypothesis that those events correspond to direct impact on the thermistor, which is not aligned with the grid of the other bolometer. Nevertheless, we have seen that *all* those high energy events are in coincidences with a small amplitude event in the second bolometer. This is attributed to the cross-talk between bolometer in a pair, as discussed in Section 3.4. The non-linearity, appearing with the curved shape in the coincidences, can be entirely explained by the saturation of the highest amplitude glitches. Nevertheless, we can evaluate the level of cross-talk as between 0.01 to 0.44% depending of the bolometer pair, for ≈ 3000 sigmas events for which the effect of saturation is small. The high amplitude events correspond to an energy of ≈ 15 keV left on the grid+thermistor by a particle, this is very close to the expected energy deposited by a 1 GeV proton on the thermistor.

3.2. Interaction with the wafer

We identify the long glitches as produced by cosmic rays hitting the silicon die. This was first indicated by the ground tests (Catalano et al. 2013), showing that the NTD thermometer is sensitive to a temperature change of the silicon die. The HFI ground-based calibration show a rate of events compatible with the cosmic rays flux at sea level over the silicon die surface and also that almost all these events are in coincidence between PSB-a and PSB-b. The understanding is the following: phonons generated by the event impact in the silicon die and produce fast rising time of the Germanium temperature, which decays with the bolometer time constant. The slow part is the thermal response of the entire silicon die temperature rising and then falling as the heat conducts out from the die to the heat sink (Catalano et al. 2013). This hypothesis is reinforced by the comparison of cumulative counts $N(>E)$ of long glitches from bolometer to bolometer which is shown in Figure 19. To make this comparison, we have normalized the counts such that we evaluated the number of event per unit of time and per unit surface of the silicon wafer (as the total surface varies from bolometer to bolometer). Also, as for short glitches, we have intercalibrated the energies of events between bolometers by matching the different counts at measured energies around 0.05 keV, which correspond to the deposited energy on the silicon die of $\approx 10^3$ keV after absolute calibration. This absolute calibration is performed such that the observed faint-end break of counts, which is clearly observed in the figure, match the expected minimum deposited energy by \sim GeV protons on the silicon die, which is ≈ 140 keV, for normal incidence, as described later. Energy calibration cannot be performed accurately from measurement due to important uncertainties of heat capacities of the silicon die. Figure 19 shows the cumulative counts for all HFI bolometers used for the scientific analysis. We clearly see that they all match in shape and amplitude with very small scatter. For energies below 20 sigmas of the noise, we have also computed the cumulative counts for all events without distinction on families (green curves in the figure), but we have already seen that long events dominate at low energy, so the total counts are representative of counts of long glitches. The faint-end break in the counts is detected without ambiguity. This is an important result since it shows that there is a limited number of low en-

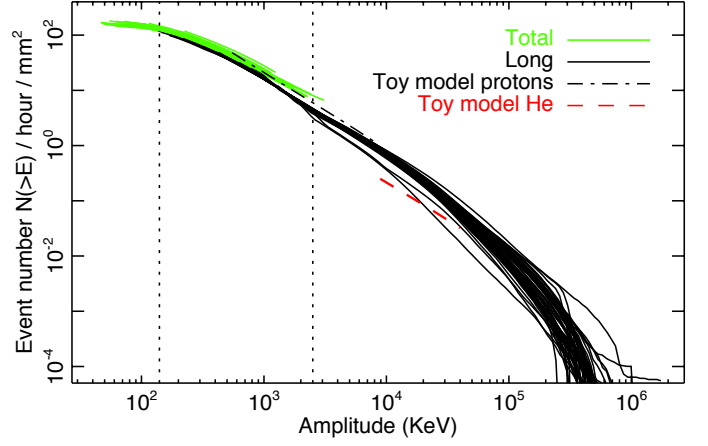


Fig. 19. Cumulative distribution $N(>E)$ of long glitches per unit surface of the wafer for all bolometers used for the scientific analysis. The black solid lines correspond to selected long glitches. The green lines correspond to total glitches, but are representative of long glitches since they dominate at low energy. A relative calibration of the energy, which indicated in the x-axis, has been for all bolometers such that the cumulative counts match at $\approx 10^3$ keV. The absolute calibration of the energy is performed such that the faint-end break of the counts match the expected deposited energy of ≈ 140 keV in the silicon die. This calibration on the model is necessary since we only measure the energy in the grid+thermistor system, and the heat capacity and link conductivities are not known with a sufficient accuracy. Also, we use the values of peak of glitches to record the glitch amplitudes which are not representative of thermal processes, as the fast part of long glitches are expected to result from ballistic phonon effects. Nevertheless, we observe that the shape of the cumulative counts match for all detectors with a low dispersion. The break of the counts at faint-end is very significantly detected. This is our best indication from flight data that long glitches result from particles hitting the bolometer silicon die. Dot dash and dash lines correspond to the predicted power law distributions of deposited energy from protons, and helium, respectively, from the toy model developed in 3.3 for sensibly energies higher than the stopping power energies. Predicted minimum deposited energies for helium and protons are indicated with dotted lines. We interpret the second apparent bump at energies ~ 20 times the energy of the break as the signature of He nuclei. The fact that we observe an excess in the counts at the expected energy of the minimum stopping power for helium reinforces our hypothesis for the origin of long glitches.

ergy glitches in data which are undetected, and would affect the cosmological results. From this limit, we measure that the total number of events penetrating the shielding of the satellite around the bolometer is about 4.5 per second and square centimetre. This is in very good agreement with the expected value in the bolometer environment computed in Section 3.1 of $\approx 5 \text{ s}^{-1} \text{ cm}^{-2}$. The slope and amplitude of the distribution can be predicted with a simple model of interaction of particle with the silicon die as shown by the toy model described in Section 3.3. Predictions are also represented in Figure 19 for primary galactic protons and Helium nuclei. We observe a very good match of the model with the data showing that particles detected by *Planck* at the energies above the faint-end break are primary galactic protons. The barely apparent second bump in cumulative counts at deposited energies ~ 3000 keV probably correspond to the contribution

from Helium nuclei, which are expected to contribute to $\approx 10\%$ of the counts at those energies. High energy galactic electrons could also contribute to the measured counts for high deposited energies

The very large scatter in the distributions of long glitches with respect to different detectors, calibrating the energy on the short distributions, as shown in Figure 18, is due to the variation of thermal links between the grid and the silicon die, as well as silicon die heat capacity, reducing or increasing the fraction of energy transmitted to the thermistor for both phonons and thermal processes. The detectors with smaller glitch counts (e.g. 143-1a and 143-5 in Figure 8) are those with smaller fraction of the energy propagating from the wafer to the grid. For those detectors we do not see the break in the counts which should be below the detection threshold. We observed that in general PSB-b have are more sensitive to long glitches than PSB-a (a few exceptions exist).

Detectors with smaller rates of glitches should have more undetected glitches than detectors with a high rate. This hypothesis is verified with the help of the cross-correlation analysis between bolometer signal from the same PSB pair described in 4.2 (see Figure 27 in particular). We observed that bolometers pairs with the smaller rate of glitches are the ones with higher correlations around 1 Hz, which is attributed to glitches below threshold. Whereas pairs for which one of the bolometer has a visible faint-end break in the counts has smaller correlation of noise. The impact on final data after processing is studied in 5.2.

We have already seen that events hitting the bolometer silicon dies must deposit a fraction of their energy, which is typically the minimum stopping power of the silicon for events close to the normal incidence and with energies of 140 keV. Then most of the events must hit instantaneously the two wafers in PSB pairs. This is compatible with what we observe in the coincidence graph shown in Figure 14, Section 2.7. Indeed, we find that between a third and half of the events are depositing the same energy in both PSB-a and PSB-b with some intrinsic dispersion. We mentioned in 2.7 that the factor of amplitude between events in signal to noise units varies from 0.25 to 4 depending on the bolometer pair, but this factor becomes 1 after recalibrating in units of deposition energy on the silicon die as expected. Furthermore, 100% of the events (at least for amplitudes higher than 300 sigmas) happen in coincidence between the two bolometer pairs but with different energy deposition, by a factor of 300 at maximum. This difference could be explained by the fact that some relatively low energy events lose a significant fraction of their energy in the first silicon die and then deposit more in the second, as the stopping power is a decreasing function of the energy for the considered particles. In principle we should have a small proportion of events hitting the corner of the bolometer wafer with no counterparts in other bolometers, but we do not have evidences of such events. A complete modeling of the interaction of particles with the two silicon dies, including accurate physical modeling of the interaction is postponed to a forthcoming publication.

Very importantly, the coincidence study indicates that the contribution to the glitches by secondary particles, like e.g., delta electrons is negligible since those low energy events would deposit all their energy in the first wafer without counterparts in the second.

The slow part of long glitches is related to the thermal relaxation of the energy. The different time constant can in principle be related to the different components of the bolometer. This will be studied in the future publication [Spencer \(2013\)](#).

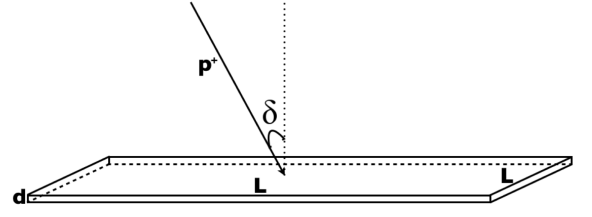


Fig. 20. Geometrical scheme of the toy model of cosmic ray interaction with the silicon die.

3.3. Toy model for interaction with the silicon die

We have developed a toy model considering the impact of cosmic rays at the second Lagrange point with the silicon die. We start with a solid square box made of silicon with the same equivalent surface of the real silicon die (see Figure 20). We consider that the side of the square is much greater than the thickness of the silicon die. The input of the model are:

- Geometrical parameters of the bolometers.
- Stopping power function and density of the silicon die.
- Energy distribution of CRs at L2 (see e.g., [Adriana 2011](#)).

By integrating over the solid angle, the surface and the integration time, we obtain an analytical equation as:

$$\frac{\Delta N}{\Delta E_{abs}} = \frac{4\pi N_0 \Delta t E_{p^+o}}{(2\gamma + \beta - 1) \cdot E_o^{\frac{\beta-1}{\gamma}}} \cdot E_{die}^{-\frac{\gamma+1-\beta}{\gamma}}, \quad (1)$$

where N_0 is the amplitude of the spectrum of incoming protons or alpha particles at L2, Δt the integration time, E_{p^+o} the reference proton energy, γ and β are the power law indexes of the fit between the stopping power function and the energy distribution of the proton at L2 respectively, $E_o = \rho_{sil} \cdot d \cdot SP(E_{p^+o})$ is the reference absorbed energy for an orthogonal impact, ρ_{sil} the density of the silicon, d the thickness of the silicon die, $SP(E_{p^+o})$ the stopping power function calculated at a reference proton energy, and E_{die} is the energy absorbed by the silicon die.

The predictions of this model for protons and alpha particles are shown in Figure 19, together with the energy spectrum measured in bolometer data. The power law index fit well with the flight data and the model is able to cover almost all the range of energies. We conclude that in terms of rate and energy distribution the thermal coupling between the silicon die and the NTD thermometer likely explain the long glitches seen in HFI in-flight data.

3.4. Cross-talk between bolometers

Very high amplitude short events in one of the bolometers from a PSB pair is always seen in coincidence with a small event in the other bolometer. This is attributed to cross-talk between bolometers. The estimated level is $\approx 10^{-3}$ as can be seen in Figure 13 for the considered bolometer pair, and varies between 0.01 to 0.44% depending of the pair. Those events show a phase shift which varies from 0.25 to 1.4 samples depending on the pair, and the transfer function of the cross-talk signal is different than the primary glitch transfer function. We observe longer time-constants than the bolometer for the cross-talk signal, which scale from 10 to 30 ms. The origin of cross-talk between detectors from the same PSB pair might be electrical or thermal. There is no clear evidence at this point.

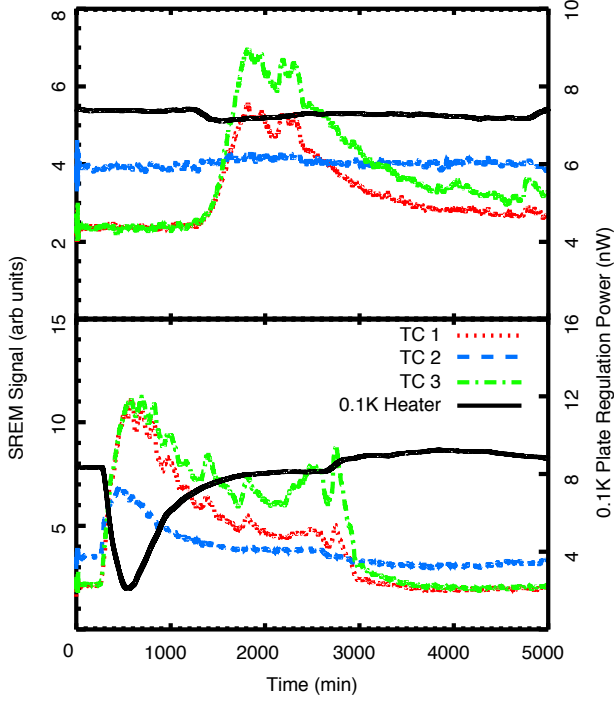


Fig. 21. output of SREM diodes TC1, TC2 and TC3 (left axis) and temperature control heater power on the 0.1K plate (right axis) and as a function of time for large solar flares on March 7 (top) and August 4 (bottom) in 2011.

We have attempted to estimate cross-talk signal between bolometers which are not mounted in the same pair. To do so we have averaged the bolometer signal at locations of detected high energy events in one of the bolometers. We found a significant but very small cross-talk signal of the order of 3×10^{-5} for some couples of detectors within the same electronics belt. However, we did not measure any significant signals in data from other bolometers, and we measured a higher limit of 3×10^{-6} .

3.5. Solar Flares

For most of the mission, solar activity was remarkably low (Mewaldt et al. 2010). In 2011, for the first time in the mission, there were several large solar flares. These flares provided a useful test signal to correlate the signal measured on the outside of the spacecraft with the SREM to signals due to particle impact on HFI. The glitch rate noticeably increases during solar flares. The heater power used to regulate the 0.1K plate decreases with increasing signal, and hence particle flux, measured by the SREM diode sensors as shown in as shown in Figure 21. The time scale of each flare was slow enough that the temperature control loop was able to compensate for the bulk heating produced by the increased particle flux as evidenced by the small phase shift of the heater power compared to the onset of signal in the SREM. Note in Figure 21 that the peak measured signal for TC1 and TC3 are only $\sim 40\%$ for the two flares. The signals of the heater power and TC2 are similar to each other in each flare. However, the peak signal of each is very different comparing the two flares. In addition, there is structure in the signal for TC1 and TC3 that are not in TC2 or the heater power response. We find that this correlation holds between the heater power and TC2 for all flares. The diode TC2 has the most shielding of the 3 diodes

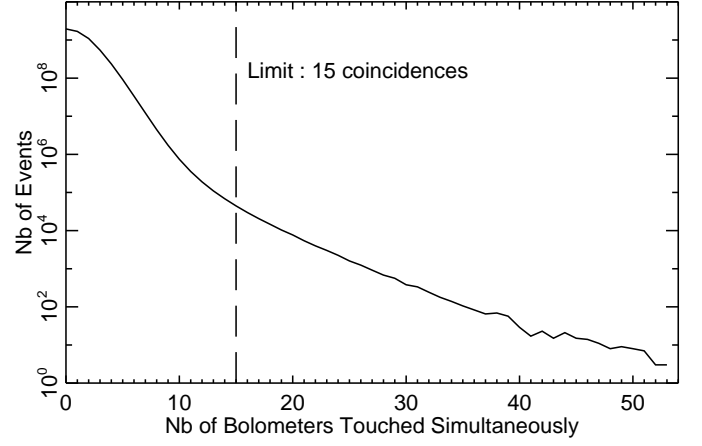


Fig. 22. Coincidence histogram (solid line) processed for the entire mission, based on the result of the glitch detection algorithm. Random coincidences dominate for low number of bolometer touched. Coincidences above 15 bolometer touched are real correlations.

in the SREM, 1.7 mm of Aluminum and 0.7 mm of Tantalum which passes only ions and protons with energies > 39 MeV. The other diodes are shielded by 0.7 mm of Aluminum for TC3 and 1.7 mm of Aluminum for TC1. This demonstrates that the spacecraft and instrument surrounding the bolometers shield particles with energies at least up to 39 MeV and all solar electrons. This is equivalent to the stopping power of ~ 1.5 cm of Aluminum (Berger et al. 2012).

3.6. High Coincidence Events

Since the beginning of the Planck survey, high temperature increases of the 0.1 K plate have been observed through the bolometers and thermometers. These events have two specific characteristics. There is a high number of glitches detected in the same time in multiple bolometers and there is an increase of the focal plane temperature of nK to μ K. In this section we will analyze the characteristics of these High Coincidence Events (HCE).

3.6.1. Detection

HCE are identified by detecting a large number of precursor glitches in coincidence in different detectors (so called "touched" bolometers) on the 0.1 K plate. These coincidences are a precursor to a temperature excursion of the 0.1 K plate. Other automated techniques that focused on finding only the temperature excursion were applied to the data, but were not successful at identifying HCE in the time stream. One reason for this is that for most of the events, this temperature rise is below the thermometry noise level.

Figure 22 shows the histogram of the number of events in coincidence for the full mission for 15 ms bins. The distribution at low number of coincidences is nearly compatible with random coincidence given the measured rate of glitches per bolometer. The distribution deviates from random coincidences above 13 bolometer touched. We set the detection threshold at 15 in order to select only real coincidences linked with HCE.

We detect $\approx 100\,000$ HCE for a number of coincidences greater than 15 or on average 5 events per hour.

3.6.2. The Different Types of HCE

For each event above the thermometry noise level we calculate separately the median of the temperature time stream for “touched” bolometers and bolometers without a precursor glitch or “untouched” bolometers. We can separate events in two categories : fast and slow, which differ in the rise time of the temperature shown in Figure 23. Depending on the type of the events, the maximum temperature value is calculated between 8–12 and 80–120 seconds after the coincidence respectively for fast and slow events.

For fast HCE, coincident glitches occur in several, but not all bolometers and are grouped together on the 0.1 K plate. The temperature rise time constant is ≈ 5 seconds. The decay time constant is ≈ 20 minutes and matches with the thermal time constant of the 0.1 K plate.

The precursor glitches for a fast HCE are short or long glitches. The separated “touched” and “untouched” bolometer temperature time stream stacking average for fast HCE greater than $1.5 \mu\text{K}$ is shown in Figure 23. The “untouched” curve rises slowly, but decays in phase with the “touched” after all bolometers thermalize with the entire 0.1 K plate. The distribution of fitted temperature amplitude for all the fast HCE (coincidences greater than 15 bolometers) obtained by template fitting is given in Figure 24 left panel. We observe that fast events above $0.8 \mu\text{K}$ are individually detected. For events detected with signal to noise less than one, we find a non-zero amplitude of $0.057 \mu\text{K}$. We also observed that the rate of fast HCE is modulated as cosmic rays over the mission.

The facts that the “touched” bolometers are grouped in the focal plane and precursor glitches of fast HCE are the same as for individual particle hits directly on the Si die (long) or grid (short), we conclude that these events are due to showers of secondary particles over part of the focal plane. The temperature increase of the 0.1 K plate results from the low energy secondary particles from the shower stopped by the bolometer plate. The rate of the most energetic events is consistent with the geometry of the 0.1 K plate and flux of Galactic cosmic rays energetic enough, $\gg \text{GeV}$, to produce such showers (Adriana 2011).

For slow HCE, the coincident precursor glitches occur in all, or nearly all, bolometers. As shown in Figure 23, there is a small temperature decrease of ≈ 1 second after the precursor glitch and before the temperature rise with a time constant of ≈ 30 seconds and, as observed for fast HCE, a decay time constant of ≈ 20 minutes. This initial decrease prior to the rise is puzzling.

The precursor glitches for these HCE are very specific and seems to be different to any categories studied in the Section 2. They have a rise time of ≈ 10 ms and a decay time which varies from event to event but of ≈ 100 ms which is a lower value from what is seen for the slow glitches (see Section 2.3). The distribution of fitted temperature amplitude for all the slow HCE is shown in Figure 24 (right panel) and the validation threshold value is $1.3 \mu\text{K}$. Slow HCE have a less steep distribution than fast HCE and dominate above $2 \mu\text{K}$. As opposed to fast HCE, we have observed that the number of slow events decrease along the mission. We use the measured thermal properties of 0.1 K plate (Planck Collaboration II 2011) to estimate that slow HCE correspond to energy deposition of $\approx 1 \text{ TeV}$ with a rate which is not consistent with the galactic cosmic ray spectrum (Adriana 2011). We have considered elastic relaxation of cracks and anomalous response of the 0.1 K stage PID loop as possible explanations. However, we have yet to reproduce a slow HCE experimentally on the flight focal plane, for example with temperature or heater steps, or in analogous ground tests. At this

time, we have not assigned a physical cause for the slow HCE events.

3.7. Particle interaction with bolometer plate

It has been shown in Planck Collaboration II (2011) that the interaction of particles with the bolometer plate are responsible of the correlated low frequency noise between bolometers. This excess noise was not seen in ground measurements (Pajot et al. 2010) and is modulated with solar activity the same as the glitch rates.

Although the mean temperatures of the 0.1 K and dilution cooler plates are stabilized with great precision, it is only at a single point near the control heater. Distributed heating from particles and other sources cause gradients within the plate. As described in Planck HFI Core Team (2011), the signal from the 2 dark bolometers was used to track the temperature of the 0.1 K plate, independent of the control thermometer. The signal from each was smoothed over a running window of 2 minutes (or ~ 2 full rotations of the spacecraft) and combined to form a thermal template which is then cross correlated with each bolometer and used to remove long term drifts from the bolometer time stream. Both the control heater power and the thermal templates are correlated with diode sensors in the SREM indicating a significant source of heating (although small $< 10 \text{ nW}$) was due to heating from interaction with the particle flux.

We have evaluated the contribution of fast HCE to the bolometer noise power spectrum. We start by assuming that the distribution of the amplitudes of fast events follows the fitted power law shown in Figure 24. Since the power law has a high index (≈ 3), some break have to be put at the low amplitude limit. By choosing a limit about 10 times lower than the amplitude such that the total counts match the detected number of coincidences for 15 bolometer touched, we found that fast HCE might account for approximately 10% of the correlated low frequency noise between bolometers. By selecting events above 15 coincidences only, we are not counting all actual coincidences since coincidence of a few bolometers, < 10 , are overwhelmed by the random events. We have tried techniques, such as fitting HCE templates over a sliding window of 0.1 K plate temperature measured by the thermal template, but have not found a one successful at detecting the bulk thermal response of the 0.1 K plate from fast HCE without the precursor coincidence flagging. However, just a modest increase in the total HCE events with < 10 bolometers in coincidence could explain all of the correlated noise. We are pursuing models and analysis techniques to quantify more accurately the number and effect of these undetected coincidences.

3.8. Other events

The origin of slow glitches is not entirely understood at this time. Lab tests using alpha particles were unsuccessful at reproducing slow glitches. Nevertheless, the similarities with long glitches suggest that both populations have the same physical origin, and that they correspond to some energy injected in the wafer. A key feature of the slow glitch is that they only occur in the PSB-a. The mechanical mounting of the PSB-a bolometer is different than the PSB-b bolometer and the SWB bolometer. Lab tests using heaters and thermometers mounted at different locations near the PSB-a are in progress to attempt to identify any unique thermal feature that could cause a slow glitch.

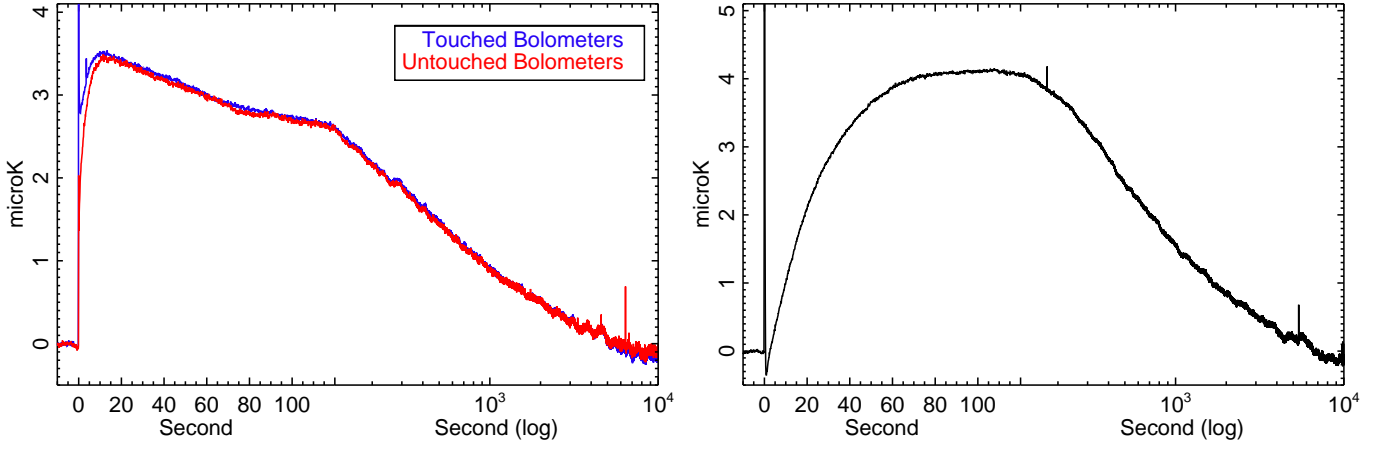


Fig. 23. Stacking of 69 fast HCE for bolometers detected as "touched" and "untouched" and 72 slow HCE for all bolometers. For fast HCE (left panel), the limit is clear, and the stacking of "untouched" bolometers gives the thermal time constant of the copper/stainless steel bolometers plate heating. For slow HCE (right panel) we observe a temperature decrement lower than $1 \mu\text{K}$ during ≈ 1 second before the temperature rising which is still not understood

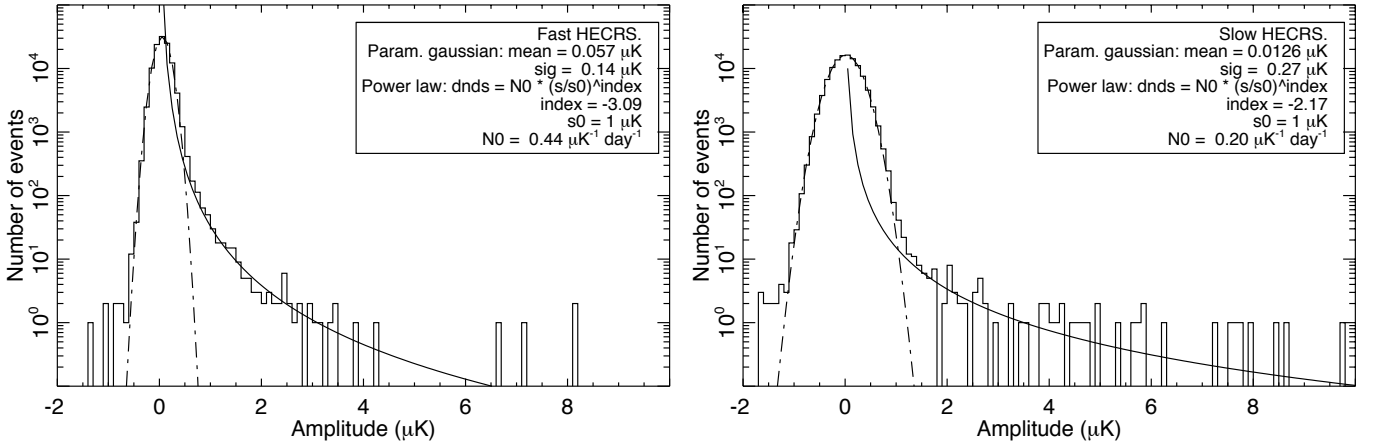


Fig. 24. Histogram of amplitudes of fast (left panel) and slow (right panel) HCE. Amplitudes are computed by joint fitting of fast and slow templates. Solid lines correspond to power laws fitted on the tails of distributions (above $1 \mu\text{K}$), the high amplitude fast events above $7 \mu\text{K}$ being removed from the fit. The number of those high amplitude fast events is not compatible with the power law distribution. Dot dashed lines are gaussians fitted on the distributions near zero amplitude and are representative of fitting errors. Parameters of the fitted distributions are given in the figure legend. Fast events (and to some extents slow HCE) have a varying temporal shape from event to event. It appears that the variation can be fitted by a contribution of the slow HCE event template. This explains in part the negative tail of the distributions of fitted amplitudes. The other reason is the confusion between events inducing an anti-correlation of amplitude parameters.

One of the bolometers (100-1a) shows another category of glitches which is not detected in any other bolometers. Those particular events have a slow response which is similar to the slow tail of short glitches, but do not show a fast decaying part. They also have a rising time-constant of ≈ 10 ms. Those events are not accounted in our glitch subtraction method and this induces a small excess in the residual power spectra at frequencies around 0.1 Hz (see Figure 26, and Section 4.2 for a discussion of the impact of such events). The excess is accounted in the total noise budget for cosmological studies (Planck Collaboration XV 2013).

Finally, precursors of slow HCE are events which are only seen in coincidence and associated with slow HCE (see Section 3.6 for a description). They are not accounted by the glitch subtraction method but are rare enough such that they do not affect data analysis.

4. Glitch Detection and Removal

A previous version of the method of detection and removal of glitches was described in detail in Planck HFI Core Team (2011). Here, we summarize the method and note the changes that have been implemented. We also show evaluation of the efficiency of the method and the impact on the noise power spectrum in the timestream.

4.1. Method

The method iterates between sky signal estimation at the ring level and glitch detection and fitting. Data are treated independently ring by ring (see Planck Collaboration I 2011, for the definition of a ring). The simple digital three-point filter (0.25, 0.05, 0.25) is used to reduce ringing around large events resulting from the electronic filter (Lamarre et al. 2010) and demodulation of

data. The three-point filter also enhances the efficiency of glitch detection since the bolometer time constant is very close to the sampling period.

4.1.1. Glitch detection and template subtraction

After estimating the sky signal as described in part 4.1.3 and removing it from the data, events above a noise threshold set at 3.2 sigmas on a sliding window of a thousand samples are detected.² On each window, a joint fit of the amplitudes of short and long glitch templates is performed simultaneously for all detected events in the window, centered at the maximum event. The short and long glitch templates are built independently of the method, and are each a sum of exponentials, three terms for short and four terms for long glitches. Templates were estimated using events detected by the method used at previous iterations of the data processing. We observed that parameters of the templates are essentially independent of the changes on the method since templates are determined using the list of detected high energy glitches which is not sensitive to the details of the processing. Consequently, iterations on the glitch template estimation was unnecessary. The method used to estimate the templates is described after presenting the main steps of the method, in 4.1.4. The joint template fitting of both short and long glitches is a main improvement as compared to the method published previously (Planck HFI Core Team 2011). It has improved the accuracy of determination of the long glitch template amplitude and led to smaller residuals from glitch in the final noise. Only one overall amplitude is used as free parameter for each glitch type and for each event.

Detected glitches are fit to the templates starting from three samples after the maximum, for small amplitude glitches in PSB-b or SWB, and is increased to eight samples after the maximum, for large amplitude glitches, and from six to eight samples in PSB-a (because of the presence of slow glitches). In order to break degeneracies between template amplitudes in case of high confusion between events, we use the prior that amplitudes are positive. The parameter fitting is performed with the analytical minimization of the χ^2 as detailed in Planck HFI Core Team (2011), Equation 2. Priors are used by fixing parameters for which the values obtained by minimizing the χ^2 is outside the authorized range. Those parameters are fixed to 0 in particular if a negative amplitude is obtained and another minimization is performed.

Slow glitches are detected as long glitches with an extremely large overall amplitude. Consequently, those events are processed by the method in the same way than long glitches with a higher fitted amplitude relative to the peak. When a slow event is detected, another iteration of the χ^2 minimization is performed, for which the long template is adapted for this event by removing the fastest exponential.

If the measured long glitch template amplitude for each event in the vicinity of the largest event is above the threshold, fixed to 0.5 times the expected amplitude for a long glitch at the measured peak amplitude, then the long glitch template is removed from the data. The expected amplitude of the long tail of glitches account for the non-linearity described in Section 2.2. To do so we use a simple empirical quadratic law which is fitted to the data, relating the glitch template amplitude and the peak amplitude. To remove the template from the data, we use the fit-

ted value of the amplitude of the long glitch template for events above 10 sigmas. Glitches with overall amplitude below 10 sigmas are treated either as long or slow glitches, and the amplitude is fixed to the expected values since 1.: the long glitches dominate at low amplitude, and 2.: the fitting errors are larger than the model uncertainties. The fitted short glitch template is not removed from the data (see discussion on the impact later).

4.1.2. Data flagging

Data in the vicinity of the peak of the long or slow events for which the fitted long glitch template is above three sigmas of the noise are flagged and are not used for the processing (and for the next event fitting). For short glitches, data for which the short glitch template is above 0.1 sigmas are flagged.

At the end of the glitch detection and subtraction, a match filter optimized to detect 2 second exponential decays is applied to the data in order to find events which are left in by the method or events for which the fit failed. This introduce an extra flagging to $\approx 0.1\%$ of the data. Additional glitch cleaning and use of different adaptive filters were found not to improve data further.

4.1.3. Sky subtraction

The sky signal is estimated at each iteration on each ring, detector by detector independently using the redundancies of measurements. Third-order spline coefficients are fit to nodes separated by 1.5 arcmin to account for sub-pixel variations which could otherwise be detected as glitch signal. Flags determined at previous iterations are used to reject data, and estimated long glitch templates are removed prior to the sky signal estimation.

Special sky estimation and glitch removal was required when scanning through or near bright objects, including planets and bright sources in the galactic plane to account for systematic errors in the subtraction of the sky signal that could be falsely flagged as glitches. These errors are due to two main effects; slow cross-scan variations of the pointing within the ring scan time, pointing uncertainties of the order of a few arcsec (Planck Collaboration VI 2013), and sub-pixel variations which are not captured by the spline coefficients.

For rings with large signal in the galactic plane, we add to the noise variance the square of a term of signal reconstruction error proportional to the signal (1% of the signal for submillimeter channels and 0.5% for cosmological channels). This automatically increases the threshold used for glitch detection at bright regions of the sky. Also, long glitch templates are not removed for high sky signal. The correction of the threshold is effective for all rings for submillimeter channels (545 and 857 GHz), and only a few percent of the data close to the galactic center for cosmological channels. Details of this treatment is described in detail in Planck HFI Core Team (2011). Furthermore, a special treatment is performed to process the data corresponding to the scanning of large amplitude planets. The motions of planets during one hour on the sky, which are mainly cross-scan, as well as the cross-scan pointing uncertainties are accounted. We fit the amplitude of the planet at each scan and rescale the averaged signal estimate on the ring with the estimated amplitude coefficient to reconstruct the sky signal, and remove the best estimate of it from the input data. This neglects main lobe beam asymmetries. However, we find that it is a good approximation at this stage given the small cross-scan shift of the planet signal during a ring time.

² The choice of 3.2 sigmas is a compromise between false event detection and glitch detection completeness as described previously (Planck HFI Core Team 2011), see Figure 7 in that reference.

Iterations between sky signal and glitch detection and subtraction are performed up to the convergence to a sufficient accuracy ring by ring. For most of them, a total of six iterations are necessary. Details of the algorithm are described in [Planck HFI Core Team \(2011\)](#).

4.1.4. Template estimation

Long and short glitch templates are fit to stacked (normalized and averaged) large amplitude events of typically 1000 sigmas of the noise. The stacked data are produced using the median value for each bin corresponding to the sampling period index after the maximum. The median is used to avoid significant contribution from other glitches. Figure 25 shows the difference between long glitch stacks and the best fit template with four exponentials in different energy windows for one bolometer (143-3a). The glitch template is determined using events with amplitudes between 1200 and 2400 noise sigmas. The difference between the stacked glitch data and the fitted template is small, but not compatible with zero reflecting the limit of the summed exponential model. The difference is systematic and of the order of 1%, which is much smaller than the fitting errors described in Section 5.2.2 (see Figure 30 in particular). So we expect that the impact of this inaccuracy on the final results is negligible. The difference between the stacks computed over different ranges of glitch amplitudes, chosen between 300 and 5000 sigmas after correcting for the non-linearity of the relative glitch tail amplitude described in 2.2, and the glitch template is as small as for the window in which the fitted template is determined. Thus, we do not see evidence of significant variations of the shape of the template with the amplitude of the glitch over a wide range. The template used for the analysis has been estimated on a limited range of energies to avoid mismatch due to the non-linearity effects. For small glitches, with amplitudes < 300 sigmas, there is a non-negligible difference between the stacked glitches and the fitted template. This is attributed to strong selection biases, e.g., Eddington bias, that affects the stacked signal, and not to real variations of the glitch template. This bias is clearly observed for stacked samples before the events which show a different mean value than a few tenth of second after the events. A systematic low frequency component is clearly visible on the stacks.

4.2. Results

The fraction of the data which are detected by the deglitching method as contaminated by glitches, and are not used for analysis goes from 6% for detectors with the lower amount of long glitches, to 20%. Figure 8 of [Planck HFI Core Team \(2011\)](#) shows a segment of data for a bolometer with high rate of glitch before and after glitch template subtraction (this was using an older version of the method, but changes are too small to be appreciated in the figure). This illustrates the necessity of removing long glitch templates from the data for an accurate determination of the cosmological signal.

The subtraction of long and slow glitch templates allows to reduce very significantly the contamination of cosmological and astrophysical signal. Figure 26 compares the power spectra of noise, orthogonal to the direction of projection on the sky, from raw three-point filtered data, with and without glitch template subtraction for all detectors from 100 to 353 GHz which are used for cosmology. Both data sets were flagged in the same way after glitch detection, and gaps are filled with white noise in addition to the result of gaussian smoothing of the data. Power spectra are

computed on data chunks of size ≈ 100 rings which are averaged to cover the nominal mission. Estimation of the sky signal has been previously removed ring by ring for each bolometer using redundancies as described in Section 4.1, and after subtracting the averaged signal for each ring to avoid filtering the noise on time-scales larger than the ring scale. Before correction, power spectra are highly contaminated by glitches at frequencies between 0.002 Hz and 2 Hz. The two-second tail is responsible of the excess between 0.01 and 0.1 Hz, while the intermediate time constant of 50 ms produces excess around 0.4 Hz, explaining why PSB-a have a higher relative excess at that frequency. We observe a very important reduction of residual noise after template subtraction. Some detectors have very few contamination from long glitches, this is the case for 143-5 and 143-1a which correspond to the two lowest spectra before correction which are seen on the top right figure. The improvement after deglitching is effective but small for those detectors as expected, and their corrected power spectra are very close to the fundamental limit of the noise. The power spectra for those detectors are then indicative of the power spectra of noise without glitches. Power spectra for other detectors seem to converge to this limit after template subtraction. Accounting from the fact that the $1/f$ part of the spectra varies in amplitude from bolometer to bolometer, we can conclude that residual contamination from glitches is below the noise at all scales for all detectors. As mentioned in 3.8, one of the 100 GHz bolometer (and only this one) has an extra family of glitches which is not accounted by our deglitching method. Some of these events are detected as “long” in the processing, and then the long glitch template is wrongly subtracted (those events are shorter than the long events). But the matched filter, designed to detect long glitch tails (either positive or negative) allows to flag segments of data when this happens, limiting the effect. The power spectrum from this bolometer is the one with the largest excess at frequencies around 0.1 Hz. This is still a small effect which is accounted in the total noise budget ([Planck Collaboration VI 2013](#)).

The comparison of power spectra of noise orthogonal to the sky projection is indicative of the quality of the correction from glitches but cannot be used to derive very accurately the contribution to the maps. The reason is that part of the noise is filtered due to the “noisy” estimation of templates by the fitting procedure which are then removed from the data. This is not the case for the signal projecting on the sky since the method iterated between sky signal and glitch detection, template fitting and subtraction. The contribution of glitches to the total power after data reduction at the map level or even at the ring level can be studied with simulations. This is done in the next section (5).

As already shown, long glitches are in coincidence between bolometers from the same PSB pair. Consequently, glitches below the detection threshold or unsubtracted tails are expected to induce residual extra correlation between bolometer timestreams from the same pair. In order to evaluate the contribution from residual glitches we have computed the cross-power spectra between bolometers. This is shown in Figure 27 between detectors at 100 GHz after averaging cross- and auto-power spectra computed on data segments of ≈ 100 rings over the full nominal mission. Sky signal has been removed and data have been processed in the same way than previously described for auto-spectra. Bolometers from the same PSB pair have an extra correlation above 0.2 Hz which is of the order of 2 to 7% of the white noise level in the spectrum for 100 GHz bolometers. The correlation degree varies from 2 to 3% for PSB pairs at 143 GHz, 1 to 4% at 217 GHz and 2 to 4% at 353 GHz. Simulations presented in the next section, show that residual noise excess is of the order

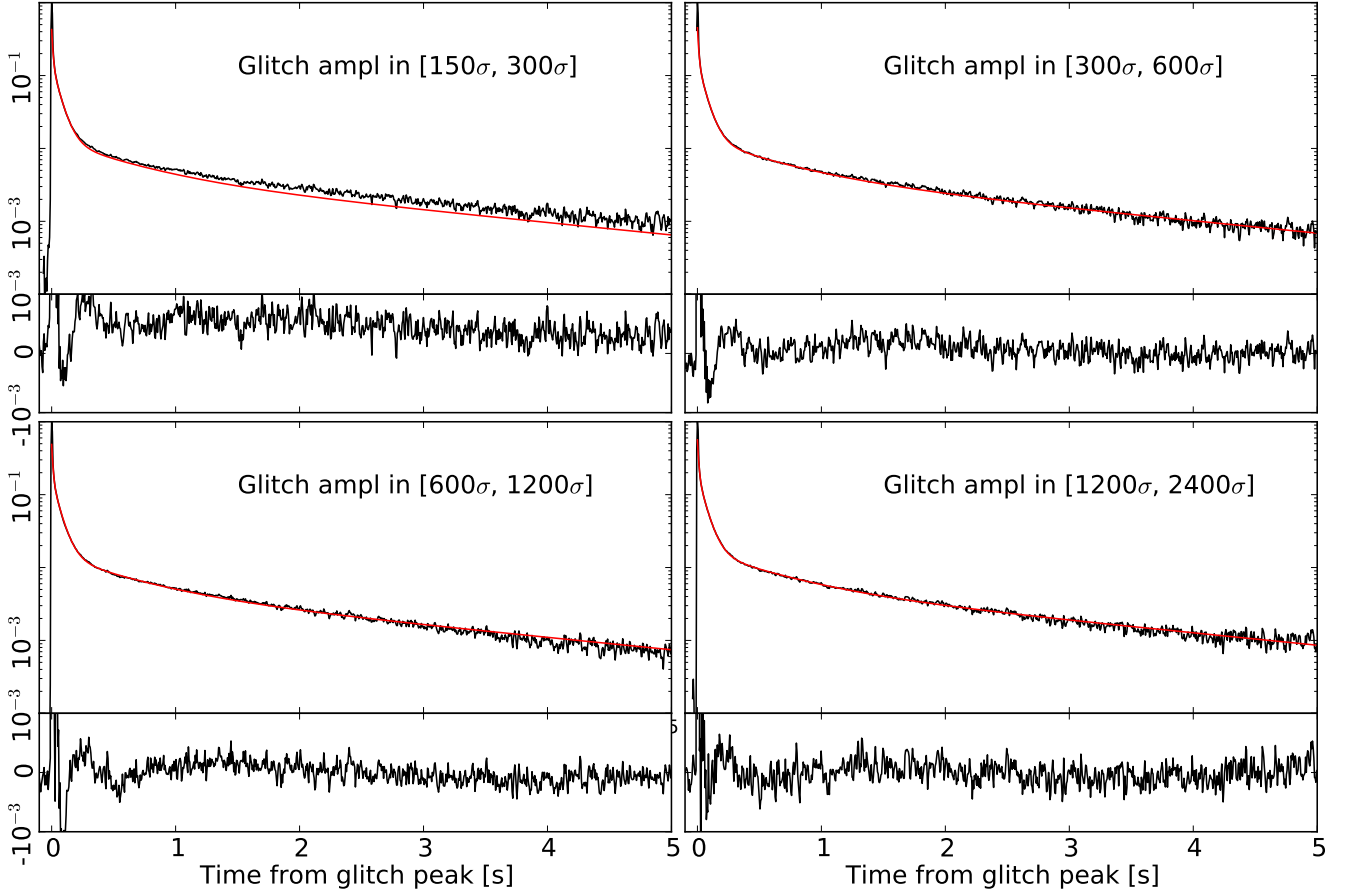


Fig. 25. Stacking of long glitches of bolometer 143-3a in different energy windows after normalizing each event to the max amplitude. The solid line correspond to the long glitch template obtained after fitting four exponentials using the data shown in the last window. The bottom plots show the difference between the stacked data and the template. We observe a good agreement between the template and the stacked data within typically 1%.

of 5% (Figure 30) given our modeling of glitches (Section 3.2), and, combined with the fact that about half of glitches have the same amplitude in PSB-a and PSB-b (Section 2.7), we should have roughly 5% correlation in the noise spectrum. This is higher but comparable to the 3% observed for this pair. The difference could be due to uncertainties in our modeling and model extrapolations. Very importantly, we observe more correlations for pairs for which both detectors have less detected long glitches; e.g., the 100-4a/4b pair for which both detectors have the lowest glitch rates, as shown in Figure 9, and which have 7% cross-correlation (as seen in Figure 27), the highest observed compared to all pairs. This is entirely explained by the fact that both detectors have then more glitches below the detection threshold, since the counts for long glitches are similar between detectors but are essentially scaled in energy as described in Section 3.2. As opposed, we observe that pairs for which the faint-end break in counts is above the detection threshold have significantly less correlations above 0.1 Hz.

We have clearly shown that glitches below the threshold are responsible from the extra-correlation of noise by averaging the two timestreams from two bolometers in the same pairs, and then by detecting events above 3.2 sigmas of the noise in the combined data. This allows to detect coincident glitches with amplitude lower by a factor $\sqrt{2}$ for about half of the events. This allowed to divide the correlated noise by a factor of 2 with only 0.1% of extra flagging of the data. This shows without ambiguity

that extra-correlation between two bolometers in PSB pairs are due to undetected long glitches below the threshold.

5. Impact of glitch residuals on final results

5.1. Simulations

In order to estimate residual contamination from glitches after processing, we have performed simulations of glitch timestream incorporating the important glitch properties we measure in data. Simulations include the following features:

- Glitches are generated with a Poisson distribution with a sub-sample resolution.
- Population spectra found in data for each population by combining bolometers, and the model explained in Section 3. In particular, for long glitches we use the measured counts for one of the submillimeter channels, which is very sensitive to long glitches, and for which we observe the break at low amplitude with a very high significance. For this bolometer, we observe rising differential counts for events very close to the threshold. The counts are extrapolated at lower flux with a constant law (this has a negligible effect). Long glitch spectra are rescaled for each bolometer by the surface of the silicon die and energy is rescaled using a factor fitted on data. Short glitch populations are derived using one reference bolometer after correcting from the effect of non-linearity on the

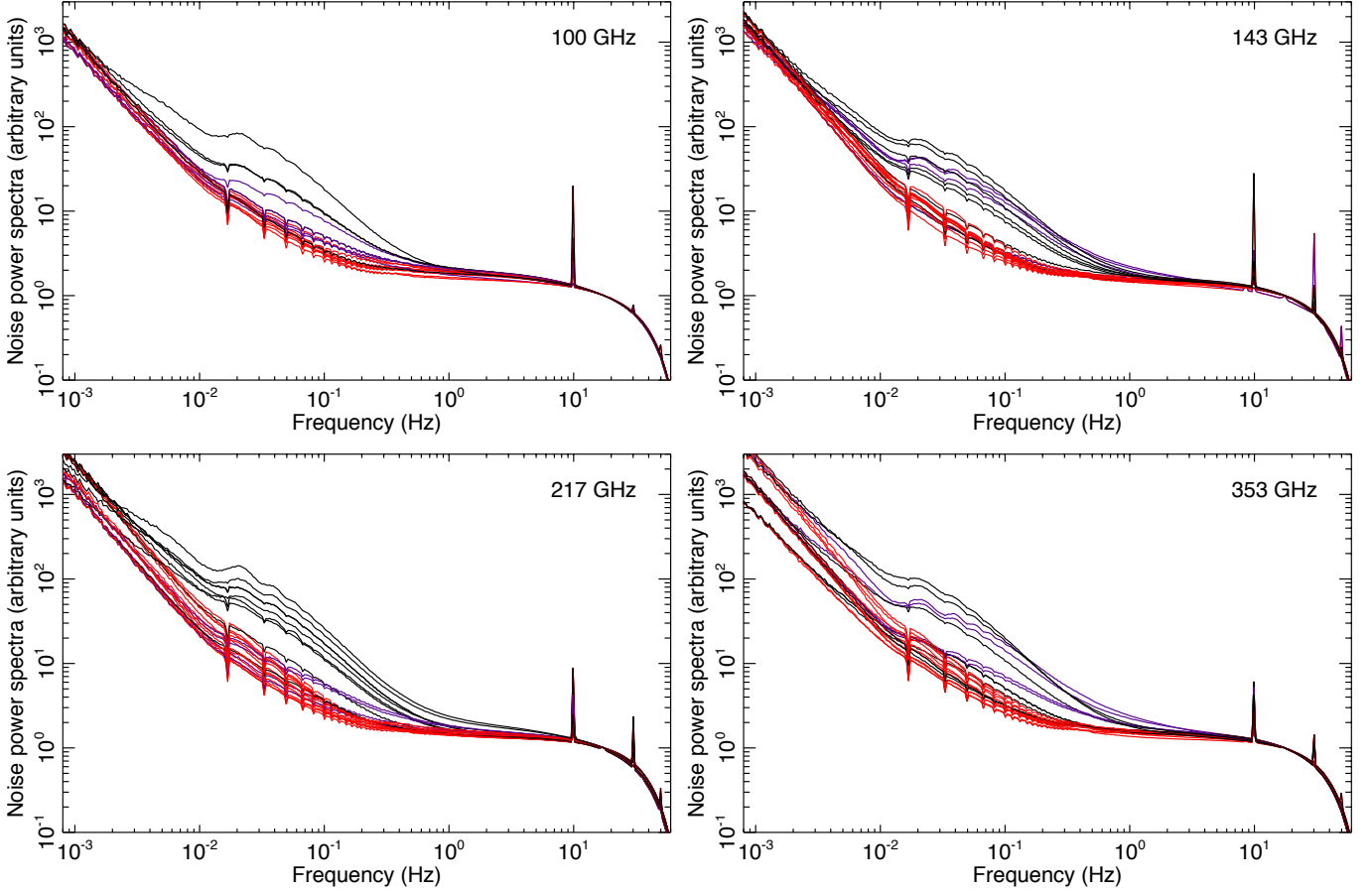


Fig. 26. Power spectra of the component of noise which do not project on the sky, for each bolometer at frequencies between 100 GHz (top left panel) to 353 GHz (bottom right panel). Black curves correspond to the power spectra without subtraction of templates for PSB-b and SWB, and the blue curves are for PSB-a. Power spectra are rescaled in amplitude such that they all match at 20 Hz. The red curves are with template subtraction. Power spectra are computed over ≈ 100 rings and are averaged over the nominal mission. Sky signal is previously subtracted from data as described in the text. This creates the narrow dips in the spectra at the harmonics of the spin frequencies. Data have been previously three-point filtered and flagged after glitch detection. The large lines on the spectra, unsubtracted at this stage, are induced by the 4 Kelvin compressor and are described in [Planck Collaboration VI \(2013\)](#). The decrease of the spectra above 10 Hz is mainly due to the three point filter applied to data. Glitches contribute to the power spectra between 0.002 Hz and 2 Hz. Power spectra of residual contamination are significantly reduced after glitch template subtraction at frequencies below a few Hertz. There is much less dispersion between power spectra from different detectors after correction - the dispersion becoming less than a factor of two - indicating that remaining contamination from glitches is not a dominant effect.

spectra by the approach discussed in Section 2.5, and low amplitude glitches below 20 sigmas of the noise are extrapolated by a power law. The spectra are rescaled in energy to match the counts measured in data for each bolometer. Slow glitch population spectra are simulated using the measurement from one of the bolometers and extrapolated using a power law at low energy. Slow glitches are simulated only for PSB-a bolometers. As for other populations, the slow glitch spectra are rescaled in energy to match the measured spectra.

- The non-linearity of the slow tail of long glitches relative to the peak amplitude as measured in data, see Section 2.2 for details.
- The temporal shape of glitches is simulated using templates for the slow parts (after ≈ 20 ms), correcting analytically the effect of the sampling average and of the three-point filter on the amplitude of the exponentials, as those are applied to data before estimation of templates. The fast part of glitches

is simulated with a full resolution, and then averaged over the sample period using a simple boxcar average.

Simulations do not include the apparent scatter of the slow tail amplitude of long glitches, apart from the intrinsic scatter due to the variations of the arrival time in the sample period reducing the amplitude in a different way. Those fluctuations does not affect strongly the performances of the method since the slow part of glitches is fitted before subtraction, and so those amplitude variations are absorbed by the fit. Moreover, we used a fixed template for short glitches, which is not realistic since we observed scatter in the slow tail, and we observed two sub-categories of short glitches. The effect of using a single, fixed template for short glitches should be very small since the short glitch template are not removed. We did not include the 2 second exponential decay in for short glitches in simulations since uncertainties in its amplitudes are important. Nevertheless we have evaluated that the contribution to the power spectrum in timestreams should be below 0.1% of the noise power spectrum

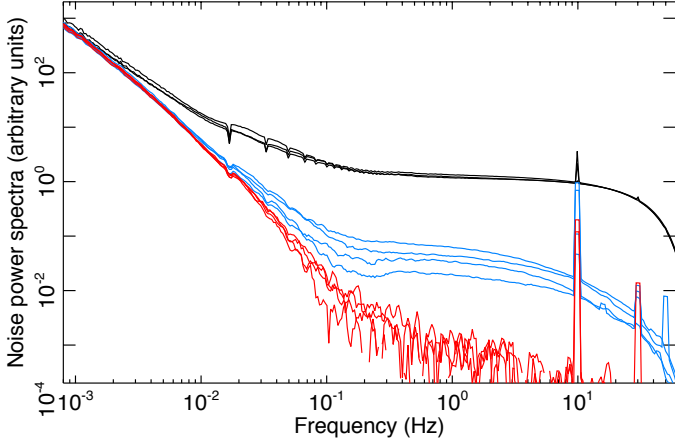


Fig. 27. Cross- and auto-power spectra between a few detectors at 100 GHz. Spectra are computed in the same way than described in Figure 26 caption. Black curves correspond to some of the auto-spectra shown in Figure 26. Data have been previously rescaled such that auto-spectra match at 20 Hz, and such that the white noise level approximately 1. Blue curves correspond to cross-spectra between detectors from the same pair. Red curves are for detectors from different pairs. The extra correlation observed for PSB pair bolometers above 0.1 Hz at the level of 2 to 7% of the white noise spectrum is due to residual glitches below the threshold. Some residual correlation at the level of $\approx 0.1\%$ at ≈ 0.2 Hz is observed between other bolometer pairs which are spatially close to each other might result from imperfect sky signal subtraction due to pointing drift, as the error is coherent between different detectors nearby. The low frequency noise is highly correlated between detectors and is due to thermal fluctuations of the focal plane.

given the population spectrum of short glitches. The effect of non-linearity of bolometers and of the ADC is not simulated. On data, the non-linearity has the effect of reducing the fast part of the glitches, which are short essentially since they dominate at very high amplitudes, relative to the slow part. We do not expect this to degrade the performances of the method since the slow part of glitches since the template fitting starts a few samples after the peak, in parts of the signal which is not affected by non-linearity. Finally, we did not implement the correlations of glitches between PSB pairs. The correlation of noise is not tested at this stage, and we treat each bolometer independently.

To the glitch generated signal, we added gaussian noise containing a white component and a low frequency component described by a power law fitted to the data (index and f_{knee}). We also added a timestream of pure signal obtained by scanning a generated CMB map, as well as galactic dust and point source maps from the *Planck* Sky Model (Delabrouille et al. 2012), using the pointing solution derived for the data. The constructed signal timestream is performed interpolating extracted signal from the map to limit sub-pixel effects (see Reinecke et al. 2006, for the methodology). We filtered the simulated data using the same three-point filter that for the data. The differential counts recovered from the simulations after processing is shown in Figure 28 for bolometer 143-2a. We observe a very good agreement with the spectra recovered in *Planck* bolometer data shown in Figure 11.

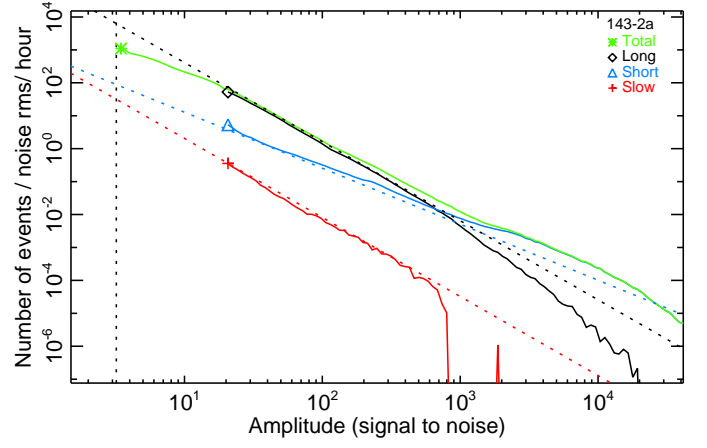


Fig. 28. Differential counts for the three populations of glitches for one of the detectors with high rate of glitches (143-2a) measured after analysing simulated data in the same way than actual data. This can be compared to the results on real data shown in Figure 11 for the same bolometer. Dashed lines are shown for reference and are identical than the lines shown for real data. We find an almost perfect agreement between simulations and real data, except for very high amplitude glitches $\geq 10^4$ sigmas. Those glitches are affected by the bolometer non-linearity in real data, and we did not simulate the effects of non-linearity in simulations, explaining the discrepancies in the counts. It also appears that we simulated slightly less very high amplitude slow glitches than in data. This concerns only ~ 1 event per day.

5.2. Error estimation

5.2.1. Evaluation of signal bias by the deglitching procedure

Due to the high signal to noise of HFI data, the sky signal subtraction is a critical part of the deglitching procedure. Errors in the sky signal estimation could easily induce spurious detections of glitches and errors in the template subtraction which would then correlate to the signal. This could bias the sky signal estimation for two main reasons; first by flagging as bad data slightly more on average when the sky signal is higher (or lower); second, by subtracting slightly more glitch templates signals when the fluctuations of the sky signal is of a given sign.

We have verified the absence of bias of the signal with the help of simulations. Indeed, we have computed signal rings by projecting pure signal timestreams used for simulations in one side, that we write $r_{0i}(p)$, where p is the ring pixel and i is the ring number, and in another side we have projected the simulated observed data from which we have subtracted estimated glitches templates after applying the deglitching procedure as performed for real data, and also after rejecting data detected as contaminated (flagging). We write this last quantity $\hat{r}_i(p)$ for data ring i . We then computed the average binned power spectrum of $r_{0i}(p)$ as:

$$P_0(q) = \frac{1}{NN_q} \sum_{i=1}^N \sum_{k \in D_q} r_{0i}(k) * r_{0i}(k)^\dagger, \quad (2)$$

where \dagger denotes the transpose conjugate, $r_{0i}(k)$ is the Fourier transform of $r_{0i}(p)$ and we summed over N rings (with N of the order of 10 000). We also computed the average cross power spectrum between $r_{0i}(p)$ and $\hat{r}_i(p)$ as:

$$P_c(q) = \frac{1}{NN_q} \sum_{i=1}^N \sum_{k \in D_q} r_{0i}(k) * \hat{r}_i(k)^\dagger. \quad (3)$$

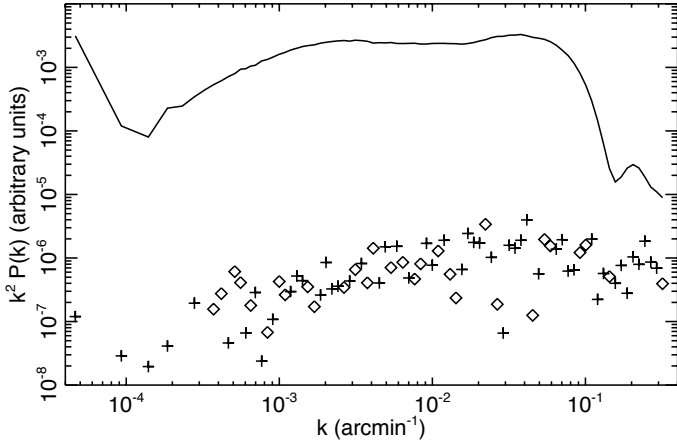


Fig. 29. Constraints on the signal bias after deglitching. Black curve: power spectrum ($k^2 P_0(k)$ in the text with k taken at the center of each bin q) of ring data after projecting pure simulated signal timestream for one of the detectors at 143 GHz (see below), containing CMB anisotropies, galactic dust and point source signal, and using the actual pointing; For the other displayed points: we computed the cross-spectrum between 1. the estimated signal on rings after subtracting long glitch templates to the simulated data and after flagging, and 2. the input signal only averaged on the same rings. Crosses and diamonds correspond to the difference between this cross-spectrum and the pure input signal power spectrum shown in black, for positive and negative points, respectively. The quantity displayed is $k^2(P_c(k) - P_0(k))$ as described in the text. We averaged the power spectra of ten thousand rings. Simulations are performed for one detector with a high rate of glitches at 143 GHz (143-2a). In the absence of bias of the signal due to the deglitching we expect that the cross-power spectrum described above is an unbiased estimate of the input signal power spectra, and then the difference should be compatible with zero. We do not detect significant bias in any of the 100 logarithmically spaced bins, and we place an upper limit of $\approx 5 \times 10^{-4}$ in each bin at the scales relevant for the CMB analysis.

In absence of bias of the signal introduced by any of the two effects previously described, $P_c(q)$ should be an unbiased estimate of $P_0(q)$:

$$P_0(q) = \langle P_c(q) \rangle, \quad (4)$$

where $\langle \cdot \rangle$ is the ensemble average over infinite number of realisations of noise and glitches.

In practice, the quantities $P_0(q)$ and $P_c(q) - P_0(q)$ are evaluated for simulations of the 143-2a detector for $N = 10\,000$ rings. We selected rings with no strong galactic signal in the galactic plane to avoid giving too much weight to the galaxy, keeping about 95% of the rings. Results are shown in Figure 29 for logarithmically spaced bins. We observe that $P_c(q) - P_0(q)$ is compatible with zero at all scales. We measure a higher limit of the bias of $\approx 5 \times 10^{-4}$ in individual bins at all scales relevant for cosmology, i.e. for k corresponding to $1 \leq \ell \leq 2000$. The absence of significant bias due to the deglitching procedure is verified at the ring level, but this conclusion can in principle be drawn at the map level and hence at the CMB power spectrum level. Also, we do not expect to observe differences for the CMB measured with other bolometers since the presence of bias has to do with the errors made on sky signal reconstruction, and not on errors made of the glitch template fitting and subtraction. Nevertheless, we have performed the same exercise for

a SWB bolometer at 143 GHz (143-5). We do not find any bias and placed an even lower limit of 2×10^{-4} due to lower rate of glitches for this bolometer.

The situation is different for strong galactic signal and for high frequency channels as the detection threshold is increased with the signal amplitude and, even, long glitch templates are not subtracted for very high sky signal, as described in Section 4.1. We expect this to bias slightly the estimation of the sky signal in the positive direction since less positive glitch signal is removed in regions of strong sky signal. This effect is described in detail in Planck HFI Core Team (2011). In particular we observed an effect of the order of 4×10^{-4} of the signal amplitude at 545 GHz. The effect on the beam response estimation is studied in detail in Planck Collaboration VII (2013).

Because the sky signal is estimated using data from individual rings, this estimation is a noisy estimate with an rms which is roughly reduced by 7 as compared to the rms of the noise in each measurement. This induces some weak correlations in the glitch detection between each circle in the ring, after the sky signal has been removed from the data. This effect does not bias the estimation of the signal as was shown before, but correlate slightly the remaining noise, after flagging and template subtraction, between subsets of data measured by taking half rings, at a level of $\approx 1\%$. We have studied this effect in detail in Planck Collaboration VI (2013) (see Table 2 and Figure 32 of this reference in particular), and it has been taken into account for the noise prediction.

5.2.2. Glitch residual contamination

We have evaluated for some bolometers the level of contamination by glitches left in data after the processing at the ring level by comparing the power spectrum of the input simulated noise projected on rings with the power spectrum of processed simulated data, after removing the input sky signal from the data. This is shown in Figure 30 for simulations of data of the same two detectors as in the previous section: 143-2a containing a high rate of long glitches; and 143-5 with a low glitch rate but consequently more glitches below the threshold (see Section 3.2), after averaging the spectra over 10 000 rings. We also compare the two power spectra previously described with the power spectra obtained without removing estimated glitch templates to the data but using the same produced flags.

For bolometer 143-2a, we can see that glitches dominate over the noise on large scales, even after flagging, for $k < 2 \times 10^{-3} \text{ arcmin}^{-1}$. We observe an important gain in the noise power spectrum after removing long glitch templates. Nevertheless, glitch residuals still contribute to the noise power at the level of 30% below $k \approx 2 \times 10^{-3} \text{ arcmin}^{-1}$ and below 10% above $k \approx 6 \times 10^{-3} \text{ arcmin}^{-1}$. We attribute the excess at low frequency to errors in the subtraction of templates. Undetected glitches below the threshold contribute significantly at higher frequencies, at the level of 5% of the power for this bolometer, and causes the observed excess for $0.03 < k < 0.1 \text{ arcmin}^{-1}$. For bolometer 143-5, the contamination by glitches before template subtraction below $k < 10^{-3} \text{ arcmin}^{-1}$ is between 15 and 20% and of the order of 8% above. After glitch template subtraction, the contamination reaches the level of 8% at almost all scales. This value corresponds to the level of contamination by undetected glitches below the threshold, which is higher than for the 143-2a bolometer in agreement with our modeling (see Section 3.2).

This study shows that the remaining contamination from glitches is below the instrumental noise level even for channels with the highest glitch rates. The evaluation of the contamina-

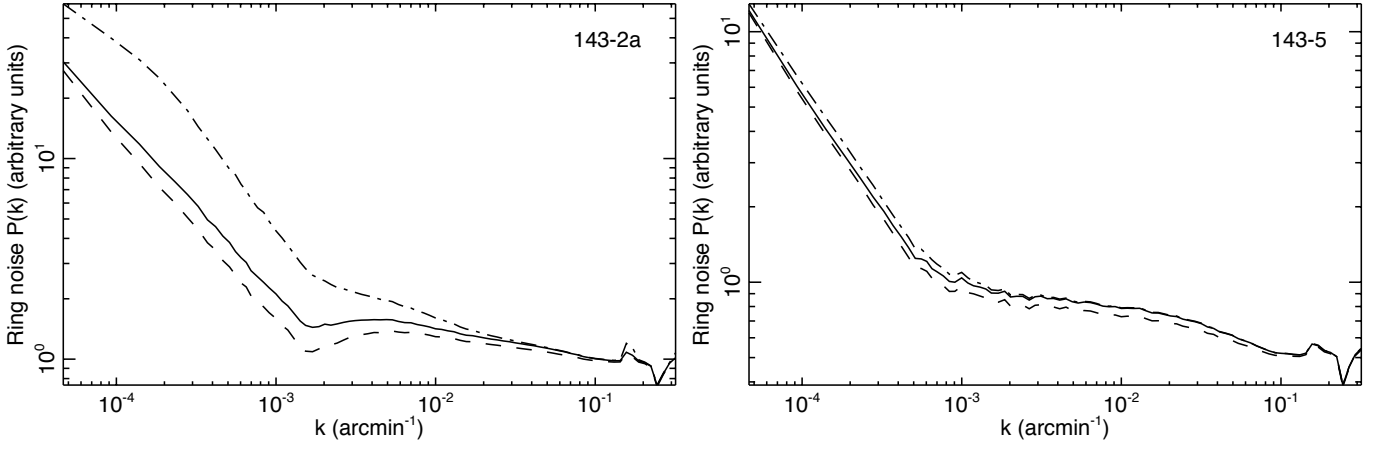


Fig. 30. Estimation of power spectra of noise residual after averaging data on rings for the 143-2a bolometer (left) and the 143-5 bolometer (right). Power spectra are averaged over 10 000 rings and are computed after removing input simulated signal to the simulated data and using the estimated flags. The dot-dashed curve is without subtraction of long glitch tails, the solid curve is with subtraction as done for real data, the dashed curve is for the same simulations but without glitches. Residual glitches are significantly reduced after template subtraction.

tion at the map level and on the CMB power spectrum has not been performed in this paper and is postponed to the release of the data of the full *Planck* mission. Nevertheless, the contribution of glitches to the errors on cosmological results (Planck Collaboration XVI 2013; Planck Collaboration XV 2013) has been accounted since noise estimation is based on survey difference maps (Planck Collaboration VI 2013).

6. Conclusions

In this paper we propose an interpretation of the glitch signal observed in *Planck*-HFI bolometer data, we present details of the glitch subtraction and flagging method, and we evaluate the impact of residual glitches in cosmological data after processing.

We observed three families of glitches, short, long and slow, where each is described by a sum of 3 or 4 exponentials. They are distinguished from each other by the relative amplitudes and time constants of the 4 terms. The rate of each glitch type is anticorrelated with solar activity indicating that they are all due to energy deposition by galactic cosmic rays. Using the response of the on board particle monitor and cryogenic stages during solar flares, we find that the spacecraft and surrounding instrument mass shields the 0.1K plate and bolometers from all particles with energies at least < 39 MeV. Short glitches have a response similar to the optical response. These short glitches result from direct particle energy deposition in the grid for the lowest energies or in the Ge thermistor for the highest energies.

Long glitches dominate the total glitch count rate, but are usually smaller in amplitude than that short glitches. Long glitches show a fast part with ~ 10 ms decaying time constant, followed by the sum of slow exponentials from ~ 50 ms to 2 seconds time constants. We find that the flux of the long glitches is the same for all bolometers, when we use the area of the Si die. Coincident counts in the PSBs paired in a single bolometer module in the flight data, as well as laboratory tests of spare bolometers on the ground using alpha sources to expose the absorber grid and Si die separately, and tests using 23 MeV proton beam line, support the conclusion that long glitches are due to particles depositing energy in the Si die. We find a minimum energy deposition in the count distribution of long glitches that corresponds to a proton with an energy at the minimum of the proton

energy loss spectrum traversing the Si die normal to the surface. This minimum deposited energy is above the noise threshold for about half of the detectors. Thus we can detect individually almost all of the glitches from the bolometer data. We suspect that the fast part is due to hot ballistic carriers propagating from the wafer to the thermistor. The slower time scale response is from the thermal relaxation of the Si wafer. We find evidence of long glitches caused by galactic cosmic ray helium but no evidence of galactic cosmic ray electrons. Low energy showers of secondary or delta electrons were suspected to be the cause of the high rate of glitches in HFI. However, the high rate in PSBs is measured in coincidence between the two bolometers. This signature cannot be caused by a delta electron shower. However, there is evidence of delta electrons in the coincidence of short glitches in PSB pairs. In this process, the delta electrons are produced when a high energy particle hits the absorber grid of one bolometer and produces coincidence glitch at high probability and at lower energy, in the neighboring grid.

Slow glitches are not understood at this time and have not been replicated yet in the laboratory. These glitches have nearly the same long time scale behavior as long glitches and thus are expected to be from energy deposition somewhere else in the module.

We detect high energy secondary showers from very high energy events both as coincidence glitch detection among many bolometers and heating of the 0.1K plate. The rate ~ 5 /hour and energy of these events is consistent with impact of galactic cosmic rays at very high energies > 1 GeV/nucleon.

We detect a second type of high energy event with a different time response than that of the secondary showers, a characteristic energy \sim TeV and at a rate that is too high to be due to cosmic rays. We currently do not have an explanation for cause of these events.

The new glitch analysis presented here is an improvement in the one previously reported. The method iterates between sky signal estimate ring by ring independently, and glitch detection above 3.2 sigmas of the noise and subtraction. The sky signal is carefully estimated before subtraction using spline interpolation to avoid spurious event detection. For a better separation of glitches into different categories, we employ for each detected event a joint fitting of the three glitch types using tem-

plates. Long and slow glitch templates are subtracted from the data. Without this subtraction, residual glitch tails after flagging would dominate over the noise in a large range of frequencies. The glitch removal method improves the noise performance of HFI, we found that the residual contribution from glitches after template subtraction is below the noise at all frequencies, and has maximum amplitude at around 0.1 Hz. Realistic simulations including the modeling of glitches support this result, and show for the two bolometer studied at 143 GHz that residual glitch contribute to less than 20% of the noise spectrum on scales along the scan larger than ≈ 2 degrees. At smaller scales the residual contribution is smaller than $\approx 5\%$ and is induced by long glitches below the threshold. This is supported by the observed correlations between the signals from bolometers in a PSB pair.

The rapid part of all detected events is flagged. Consequently, the amount of data rejected for the analysis varies from 8% to 20% depending on the bolometer.

With the help of the simulations, we have evaluated potential biases introduced by the method on the sky signal estimation. We did not find evidence of bias on cosmological signal and we estimated an upper limit of 10^{-4} on the spectrum.

Acknowledgements. Planck is a project of the European Space Agency - ESA - with instruments provided by two scientific Consortia funded by ESA member states (in particular the lead countries: France and Italy) with contributions from NASA (USA), and telescope reflectors provided in a collaboration between ESA and a scientific Consortium led and funded by Denmark.

The development of Planck has been supported by: ESA; CNES and CNRS/INSU-IN2P3-INP (France); ASI, CNR, and INAF (Italy); NASA and DoE (USA); STFC and UKSA (UK); CSIC, MICINN, JA and RES (Spain); Tekes, AoF and CSC (Finland); DLR and MPG (Germany); CSA (Canada); DTU Space (Denmark); SER/SSO (Switzerland); RCN (Norway); SFI (Ireland); FCT/MCTES (Portugal); and PRACE (EU). A description of the Planck Collaboration and a list of its members, including the technical or scientific activities in which they have been involved, can be found at http://www.sciops.esa.int/index.php?project=planck&page=Planck_Collaboration.

References

Adriana, O. e. 2011, *Science*, 332, 69
 Berger, M., Coursey, J., Zucker, M., & Chang, J. 2012, ESTAR, PSTAR, and ASTAR: Computer Programs for Calculating Stopping-Power and Range Tables for Electrons, Protons, and Helium Ions (version 1.2.3)
 Bobik, P., Boella, G., Boschini, M., et al. 2012, *ApJ*, 745, 1
 Catalano et al. 2013, In preparation
 Crill, B. P., Ade, P. A. R., Artusa, D. R., et al. 2003, *ApJS*, 148, 527
 Delabrouille, J., Betoule, M., Melin, J.-B., et al. 2012, *ArXiv e-prints*
 Gleeson, L. & Axford, W. 1968, *ApJ*, 154, 1011
 Holmes, W. A., Bock, J. J., Crill, B. P., et al. 2008, *Appl. Opt.*, 47, 5996
 Jarosik, N., Barnes, C., Greason, M. R., et al. 2007, *ApJS*, 170, 263
 Jones, W. C., Montroy, T. E., Crill, B. P., et al. 2007, *A&A*, 470, 771
 Lamarre, J., Puget, J., Ade, P. A. R., et al. 2010, *A&A*, 520, A9+
 Masi, S., Ade, P. A. R., Bock, J. J., et al. 2006, *A&A*, 458, 687
 Mewaldt, R., Davis, A., Lave, R., et al. 2010, *Ap. J. Lett.*, 723, L1
 Mohammadzadeh, A. and Evans, H., Nieminen, P., Daly, E., et al. 2003, *IEEE Transactions on Nuclear Science*, 50, 2272
 Pajot, F., Ade, P. A. R., Beney, J., et al. 2010, *A&A*, 520, A10+
 Planck Collaboration I. 2011, *A&A*, 536, A1
 Planck Collaboration I. 2013, In preparation
 Planck Collaboration II. 2011, *A&A*, 536, A2
 Planck Collaboration VI. 2013, In preparation
 Planck Collaboration VII. 2013, In preparation
 Planck Collaboration XV. 2013, In preparation
 Planck Collaboration XVI. 2013, In preparation
 Planck HFI Core Team. 2011, *A&A*, 536, A6
 Reinecke, M., Dolag, K., Hell, R., Bartelmann, M., & Enßlin, T. A. 2006, *A&A*, 445, 373
 Spencer, L. D. 2013, *Appl. Opt.*, in preparation
 Usokin, I., Bazilevskaya, G., & Kovaltsov, G. 2011, *J. Geophys. R.*, 116, 1
 Wiedenbeck, M., Davis, A., Leske, R., et al. 2005, in 29th International Cosmic Ray Conference Pune, Vol. 00, 101–104

1 APC, AstroParticule et Cosmologie, Université Paris Diderot, CNRS/IN2P3, CEA/Irfu, Observatoire de Paris, Sorbonne Paris Cité, 10, rue Alice Domon et Léonie Duquet, 75205 Paris Cedex 13, France
 2 Aalto University Metsähovi Radio Observatory, Metsähovintie 114, FIN-02540 Kylmäla, Finland
 3 African Institute for Mathematical Sciences, 6-8 Melrose Road, Muizenberg, Cape Town, South Africa
 4 Agenzia Spaziale Italiana Science Data Center, c/o ESRIN, via Galileo Galilei, Frascati, Italy
 5 Agenzia Spaziale Italiana, Viale Liegi 26, Roma, Italy
 6 Astrophysics Group, Cavendish Laboratory, University of Cambridge, J J Thomson Avenue, Cambridge CB3 0HE, U.K.
 7 Astrophysics & Cosmology Research Unit, School of Mathematics, Statistics & Computer Science, University of KwaZulu-Natal, Westville Campus, Private Bag X54001, Durban 4000, South Africa
 8 Atacama Large Millimeter/submillimeter Array, ALMA Santiago Central Offices, Alonso de Cordova 3107, Vitacura, Casilla 763 0355, Santiago, Chile
 9 CITA, University of Toronto, 60 St. George St., Toronto, ON M5S 3H8, Canada
 10 CNRS, IRAP, 9 Av. colonel Roche, BP 44346, F-31028 Toulouse cedex 4, France
 11 California Institute of Technology, Pasadena, California, U.S.A.
 12 Centre for Theoretical Cosmology, DAMTP, University of Cambridge, Wilberforce Road, Cambridge CB3 0WA U.K.
 13 Centro de Estudios de Física del Cosmos de Aragón (CEFCA), Plaza San Juan, 1, planta 2, E-44001, Teruel, Spain
 14 Computational Cosmology Center, Lawrence Berkeley National Laboratory, Berkeley, California, U.S.A.
 15 DSM/Irfu/SPP, CEA-Saclay, F-91191 Gif-sur-Yvette Cedex, France
 16 DTU Space, National Space Institute, Technical University of Denmark, Elektrovej 327, DK-2800 Kgs. Lyngby, Denmark
 17 Département de Physique Théorique, Université de Genève, 24, Quai E. Ansermet, 1211 Genève 4, Switzerland
 18 Departamento de Física Fundamental, Facultad de Ciencias, Universidad de Salamanca, 37008 Salamanca, Spain
 19 Departamento de Física, Universidad de Oviedo, Avda. Calvo Sotelo s/n, Oviedo, Spain
 20 Department of Astronomy and Astrophysics, University of Toronto, 50 Saint George Street, Toronto, Ontario, Canada
 21 Department of Astrophysics/IMAPP, Radboud University Nijmegen, P.O. Box 9010, 6500 GL Nijmegen, The Netherlands
 22 Department of Electrical Engineering and Computer Sciences, University of California, Berkeley, California, U.S.A.
 23 Department of Physics and Astronomy, Dana and David Dornsife College of Letter, Arts and Sciences, University of Southern California, Los Angeles, CA 90089, U.S.A.
 24 Department of Physics and Astronomy, University College London, London WC1E 6BT, U.K.
 25 Department of Physics, Gustaf Hållströmin katu 2a, University of Helsinki, Helsinki, Finland
 26 Department of Physics, Princeton University, Princeton, New Jersey, U.S.A.
 27 Department of Physics, University of California, One Shields Avenue, Davis, California, U.S.A.
 28 Department of Physics, University of California, Santa Barbara, California, U.S.A.
 29 Department of Physics, University of Illinois at Urbana-Champaign, 1110 West Green Street, Urbana, Illinois, U.S.A.
 30 Dipartimento di Fisica e Astronomia G. Galilei, Università degli Studi di Padova, via Marzolo 8, 35131 Padova, Italy
 31 Dipartimento di Fisica e Scienze della Terra, Università di Ferrara, Via Saragat 1, 44122 Ferrara, Italy
 32 Dipartimento di Fisica, Università La Sapienza, P. le A. Moro 2, Roma, Italy

- 33 Dipartimento di Fisica, Università degli Studi di Milano, Via Celoria, 16, Milano, Italy
- 34 Dipartimento di Fisica, Università degli Studi di Trieste, via A. Valerio 2, Trieste, Italy
- 35 Dipartimento di Fisica, Università di Roma Tor Vergata, Via della Ricerca Scientifica, 1, Roma, Italy
- 36 Discovery Center, Niels Bohr Institute, Blegdamsvej 17, Copenhagen, Denmark
- 37 European Southern Observatory, ESO Vitacura, Alonso de Cordova 3107, Vitacura, Casilla 19001, Santiago, Chile
- 38 European Space Agency, ESAC, Planck Science Office, Camino bajo del Castillo, s/n, Urbanización Villafranca del Castillo, Villanueva de la Cañada, Madrid, Spain
- 39 European Space Agency, ESTEC, Keplerlaan 1, 2201 AZ Noordwijk, The Netherlands
- 40 Helsinki Institute of Physics, Gustaf Hållströmin katu 2, University of Helsinki, Helsinki, Finland
- 41 INAF - Osservatorio Astrofisico di Catania, Via S. Sofia 78, Catania, Italy
- 42 INAF - Osservatorio Astronomico di Padova, Vicolo dell'Osservatorio 5, Padova, Italy
- 43 INAF - Osservatorio Astronomico di Roma, via di Frascati 33, Monte Porzio Catone, Italy
- 44 INAF - Osservatorio Astronomico di Trieste, Via G.B. Tiepolo 11, Trieste, Italy
- 45 INAF/IASF Bologna, Via Gobetti 101, Bologna, Italy
- 46 INAF/IASF Milano, Via E. Bassini 15, Milano, Italy
- 47 INFN, Sezione di Bologna, Via Imerio 46, I-40126, Bologna, Italy
- 48 INFN, Sezione di Roma 1, Università di Roma Sapienza, Piazzale Aldo Moro 2, 00185, Roma, Italy
- 49 IPAG: Institut de Planétologie et d'Astrophysique de Grenoble, Université Joseph Fourier, Grenoble 1 / CNRS-INSU, UMR 5274, Grenoble, F-38041, France
- 50 IUCAA, Post Bag 4, Ganeshkhind, Pune University Campus, Pune 411 007, India
- 51 Imperial College London, Astrophysics group, Blackett Laboratory, Prince Consort Road, London, SW7 2AZ, U.K.
- 52 Infrared Processing and Analysis Center, California Institute of Technology, Pasadena, CA 91125, U.S.A.
- 53 Institut Néel, CNRS, Université Joseph Fourier Grenoble I, 25 rue des Martyrs, Grenoble, France
- 54 Institut Universitaire de France, 103, bd Saint-Michel, 75005, Paris, France
- 55 Institut d'Astrophysique Spatiale, CNRS (UMR8617) Université Paris-Sud 11, Bâtiment 121, Orsay, France
- 56 Institut d'Astrophysique de Paris, CNRS (UMR7095), 98 bis Boulevard Arago, F-75014, Paris, France
- 57 Institute for Space Sciences, Bucharest-Magurale, Romania
- 58 Institute of Astronomy and Astrophysics, Academia Sinica, Taipei, Taiwan
- 59 Institute of Astronomy, University of Cambridge, Madingley Road, Cambridge CB3 0HA, U.K.
- 60 Institute of Theoretical Astrophysics, University of Oslo, Blindern, Oslo, Norway
- 61 Instituto de Física de Cantabria (CSIC-Universidad de Cantabria), Avda. de los Castros s/n, Santander, Spain
- 62 Jet Propulsion Laboratory, California Institute of Technology, 4800 Oak Grove Drive, Pasadena, California, U.S.A.
- 63 Jodrell Bank Centre for Astrophysics, Alan Turing Building, School of Physics and Astronomy, The University of Manchester, Oxford Road, Manchester, M13 9PL, U.K.
- 64 Kavli Institute for Cosmology Cambridge, Madingley Road, Cambridge, CB3 0HA, U.K.
- 65 LAL, Université Paris-Sud, CNRS/IN2P3, Orsay, France
- 66 LERMA, CNRS, Observatoire de Paris, 61 Avenue de l'Observatoire, Paris, France
- 67 Laboratoire AIM, IRFU/Service d'Astrophysique - CEA/DSM - CNRS - Université Paris Diderot, Bât. 709, CEA-Saclay, F-91191 Gif-sur-Yvette Cedex, France
- 68 Laboratoire Traitement et Communication de l'Information, CNRS (UMR 5141) and Télécom ParisTech, 46 rue Barrault F-75634 Paris Cedex 13, France
- 69 Laboratoire de Physique Subatomique et de Cosmologie, Université Joseph Fourier Grenoble I, CNRS/IN2P3, Institut National Polytechnique de Grenoble, 53 rue des Martyrs, 38026 Grenoble cedex, France
- 70 Laboratoire de Physique Théorique, Université Paris-Sud 11 & CNRS, Bâtiment 210, 91405 Orsay, France
- 71 Lawrence Berkeley National Laboratory, Berkeley, California, U.S.A.
- 72 Max-Planck-Institut für Astrophysik, Karl-Schwarzschild-Str. 1, 85741 Garching, Germany
- 73 McGill Physics, Ernest Rutherford Physics Building, McGill University, 3600 rue University, Montréal, QC, H3A 2T8, Canada
- 74 National University of Ireland, Department of Experimental Physics, Maynooth, Co. Kildare, Ireland
- 75 Niels Bohr Institute, Blegdamsvej 17, Copenhagen, Denmark
- 76 Observational Cosmology, Mail Stop 367-17, California Institute of Technology, Pasadena, CA, 91125, U.S.A.
- 77 Optical Science Laboratory, University College London, Gower Street, London, U.K.
- 78 SB-ITP-LPPC, EPFL, CH-1015, Lausanne, Switzerland
- 79 SISSA, Astrophysics Sector, via Bonomea 265, 34136, Trieste, Italy
- 80 School of Physics and Astronomy, Cardiff University, Queens Buildings, The Parade, Cardiff, CF24 3AA, U.K.
- 81 Space Sciences Laboratory, University of California, Berkeley, California, U.S.A.
- 82 Special Astrophysical Observatory, Russian Academy of Sciences, Nizhnij Arkhyz, Zelenchukskiy region, Karachai-Cherkessian Republic, 369167, Russia
- 83 Stanford University, Dept of Physics, Varian Physics Bldg, 382 Via Pueblo Mall, Stanford, California, U.S.A.
- 84 Sub-Department of Astrophysics, University of Oxford, Keble Road, Oxford OX1 3RH, U.K.
- 85 Theory Division, PH-TH, CERN, CH-1211, Geneva 23, Switzerland
- 86 UPMC Univ Paris 06, UMR7095, 98 bis Boulevard Arago, F-75014, Paris, France
- 87 Université de Toulouse, UPS-OMP, IRAP, F-31028 Toulouse cedex 4, France
- 88 University of Granada, Departamento de Física Teórica y del Cosmos, Facultad de Ciencias, Granada, Spain
- 89 University of Miami, Knight Physics Building, 1320 Campo Sano Dr., Coral Gables, Florida, U.S.A.
- 90 Warsaw University Observatory, Aleje Ujazdowskie 4, 00-478 Warszawa, Poland